Article

Assessment of Potential Potable Water Reserves in Islamabad, Pakistan Using Vertical Electrical Sounding Technique

Mehboob ur Rashid [1,2,3,*], Muhammad Kamran [1], Muhammad Jawad Zeb [1], Ihtisham Islam [2,4], Hammad Tariq Janjuhah [4] and George Kontakiotis [5,*]

1   Geoscience Advance Research Labs, Geological Survey of Pakistan, Islamabad 44000, Pakistan; kamranchughtai.85@gmail.com (M.K.); mjawadpkpk@gmail.com (M.J.Z.)
2   National Center of Excellence in Geology, University of Peshawar, Peshawar 25130, Pakistan; ihtisham.islam@sbbu.edu.pk
3   Graduate School of Science and Engineering, Kagoshima University, Kagoshima 890-0065, Japan
4   Department of Geology, Shaheed Benazir Bhutto University, Sheringal Dir Upper 18050, Pakistan; hammad@sbbu.edu.pk
5   Department of Historical Geology-Paleontology, Faculty of Geology and Geoenvironment, School of Earth Sciences, National and Kapodistrian University of Athens, Panepistimiopolis, Zografou, 15784 Athens, Greece
*   Correspondence: mehboobgeo89@gmail.com (M.u.R.); gkontak@geol.uoa.gr (G.K.)

Abstract: This study aimed to investigate the potential reserves of potable water in Islamabad, Pakistan, considering the alarming depletion of water resources. A detailed vertical electrical sounding (VES) survey was conducted in two main localities: Bara Kahu (Area 1) and Aabpara to G-13 (Area 2), based on accessibility, time, and budget constraints. A total of 23 VES measurements were performed, with 13 in Area 1 and 10 in Area 2, reaching a maximum depth of 500 m. Geologs and pseudosections were generated to assess lithological variations, aquifer conditions, and resistivity trends with depth. Statistical distribution of resistivity (SDR), hydraulic parameters, true resistivity, macroanisotropy, aquifer depth and thickness, and linear regression (R^2) curves were calculated for both areas, providing insights into the aquifer conditions. The results revealed that the study areas predominantly consisted of sandy lithology as the aquifer horizon, encompassing sandstone, sandy clay, and clayey sand formations. Area 2 exhibited a higher presence of clayey horizons, and aquifers were generally deeper compared to Area 1. The aquifer thickness ranged from 10 m to 200 m, with shallow depths ranging from 10 m to 60 m and deeper aquifers exceeding 200 m. Aquifers in Area 1 were mostly semi-confined, while those in Area 2 were predominantly unconfined and susceptible to recharge and potential contamination. The northwest–southeast side of Area 1 exhibited the highest probability for ground resource estimation, while in Area 2, the northeast–southwest side displayed a dominant probability. The study identified a probable shear zone in Area 2, indicating lithological differences between the northeast and southwest sides with a reverse sequence. Based on the findings, it is recommended that the shallow aquifers in Area 1 be considered the best potential reservoir for water supply. In contrast, deeper drilling is advised in Area 2 to ensure a long-lasting, high-quality water supply. These results provide valuable information for water resource management and facilitate sustainable water supply planning and decision making in Islamabad, Pakistan.

Keywords: potable water; vertical electrical sounding; aquifer; lithology; resistivity; groundwater resource estimation; Islamabad; Pakistan

1. Introduction

Water is a fundamental and essential renewable resource to sustain life and all other activities on Earth [1,2]. Out of the total water present on Earth, which amounts to approximately 70%, only a mere 3% is classified as freshwater and suitable for drinking purposes [3]. Approximately 2% of the freshwater supply is held within glaciers and ice caps, leaving only 1% available for drinking, sourced from lakes, rivers and deep

aquifers [4]. Global freshwater scarcity has worsened due to climate change, population growth, increased demand, and poor management, impacting around 4 billion people globally [5,6]. According to UNICEF and WHO, around 2.2 billion people do not have access to safe drinkable water and the scenario worsens every year [6]. The scarcity of water is exacerbated by the contamination of freshwater, which can occur naturally or anthropogenically, intensifying the overall situation [6,7]. Groundwater, a vital freshwater source for one-third of the global population, is crucial for sustainable development and ensuring a reliable, renewable drinking water supply [8,9]. Groundwater recharge occurs through rivers and precipitation, providing a potential source for groundwater supply [10,11]. The groundwater is facing a pressing menace from both contamination and overexploitation within urbanized zones [12,13]. Contamination sources emanate from either human activities or industrial processes, significantly compromising water quality [8,14,15]. Once the groundwater aquifer is tainted, restoration becomes an arduous endeavor, if not an impossible one [16]. The relentless urban demand for water exacerbates the situation, causing the aquifer to deplete to the point of desiccation [17]. Exploring groundwater through the application of advanced hydrological and geophysical methods is essential to address the current demand and supply chain requirements for water resources [18,19].

Geoelectrical methods are widely utilized for the exploration of groundwater resources, as the geoelectrical properties are related to groundwater properties, lithology, chemistry, and porosity [20–23]. The geoelectrical resistivity method is a cost-effective and easily accessible method for evaluating groundwater before investing in drilling [22,24]. The measured resistivity not only gives the presence of an aquifer but also gives information about groundwater quality [24–26]. Vertical electrical sounding (VES) using the principle of resistivity gives reliable results about the groundwater, contamination, and lithological conditions based on resistivity contrast [27–33]. The progression of technology has led to the extensive acknowledgment of geoelectrical methods for groundwater detection, offering time, cost, and labor savings, along with improved drilling precision [34–36].

Pakistan is the fifth most populous country in the world with a population of 220 million and is facing water scarcity factors due to its unprecedented growth rate, urbanization, and inadequate planning [37–39]. The per capita water availability in Pakistan has witnessed a significant decline from 5260 m^3 in 1951 to 1000 m^3 in 2016 [40]. Furthermore, it is projected to further decrease to 860 m^3 by 2025, indicating a transition from water scarcity to a water-stress country [41]. Pakistan's current water supply stands at 191 Million Acre Feet (MAF), and this is projected to increase to 274 MAF by 2025, leaving a considerable gap of 83 MAF [42]. In Pakistan, two-thirds of households drink contaminated water with 30–40% of fatalities and diseases associated with water, including 53,000 deaths of children due to diarrhea [43–45]. The 20 million inhabitants of Karachi need 1100 million gallons of water per day while they are getting 450 to 480 million gallons; similarly, in Lahore, the demand is 50–55 MAF, with a total recharge of 40–45 MAF [46]. The water supply in Islamabad Capital Territory is managed through Simly and Khanpur Dam, with 30% coming from groundwater [47]. The peak supply of 141 million m^3 is insufficient to meet the 407 million m^3 demand, causing a shortage of 110 million m^3 [47]. Islamabad's urban population has grown by 1.59%, but water resources remain unaltered, causing a widening supply–demand gap with groundwater depletion of 1 m/yr [47,48]. Population growth and groundwater extraction in Rawalpindi and Islamabad have led to a rise in subsidence levels, from −69 mm/yr to −98 mm/yr between 2019 and 2020 [49]. The demand and supply of water in Pakistan are expected to worsen in the near future [38,39,50]. Water management in Pakistan is a complex challenge due to the involvement of multiple sectors, making it a difficult task to establish consensus within the water domain [39,40,51,52]. Conservation, exploration of new resources, and accurate estimation of groundwater reserves are essential for ensuring the availability of fresh water in the future [10,11]. It is crucial to take proactive measures to manage this impending water crisis in Pakistan. Advanced geophysical methods play a vital role in delineating and assessing potential groundwater reserves [53–55].

This research contributes to support the realization of UN Sustainable Development Goal 6 (SDG-6) concerning access to clean water and sanitation. The study aims to identify a deep hard rock aquifer for sustainable supply in Islamabad, Pakistan's capital territory, addressing SDG-6. The objective is focused on (i) identifying aquifers up to 500 m, (ii) delineating potential aquifer horizons, and (iii) aquifer distribution maps in selected areas of Islamabad. The hard rock aquifer in Islamabad territory has not undergone a comprehensive vertical electrical sounding (VES) survey to date in detailed work undertaken so far [56,57].

2. Study Area

The study area of Islamabad is located in the Potwar plateau within the NW Himalayan Fold and Thrust Belt of Pakistan. It is bounded by the Main Mantle Thrust (MMT) and Salt Range Thrust (SRT) to the north and south, respectively [58]. The eastern boundary is marked by the Hazara Kashmir Syntaxes (HKS), while the western side is dominated by the Margalla, Hazara and the Kalachitta ranges [59] (Figure 1a). The study area is divided into three structural zones: (i) highly folded Jurassic to Eocene limestone along the Hazara fault zone, (ii) a southward sloping piedmont bench underlain by the Rawalpindi group succession, and (iii) the Soan syncline in the southernmost part with the Soan River flowing along its axis [60]. The complex tectonics and geology of Islamabad result from the collision of the Eurasian and Indian plates, leading to the deposition of a sedimentary sequence ranging from the Jurassic to recent times. The depositional sequence is characterized by two distinct periods: a slow deposition phase (150–24 million years ago) with marine successions and minimal tectonic disturbance, followed by a fast deposition phase (24 million years ago to 1.9 million years ago) characterized by continental clastic sediments, intense tectonics, and high erosion rates [61–63]. The geological units exposed in the study area are mostly Potwar clay (clay and gravel), lei conglomerate (clay and silt), and soan formation (conglomerate, sandstone, clay stone, and siltstone) [64,65]. The complex tectonics and geology of Islamabad pose challenges for water recharge and storage capabilities [59,64–68]. The study focuses on conducting resistivity surveys at Bara Kahu and Aabpara-G13 sites to comprehend the deeper aquifer's potential, considering accessibility, time, and budget constraints (Figure 1b).
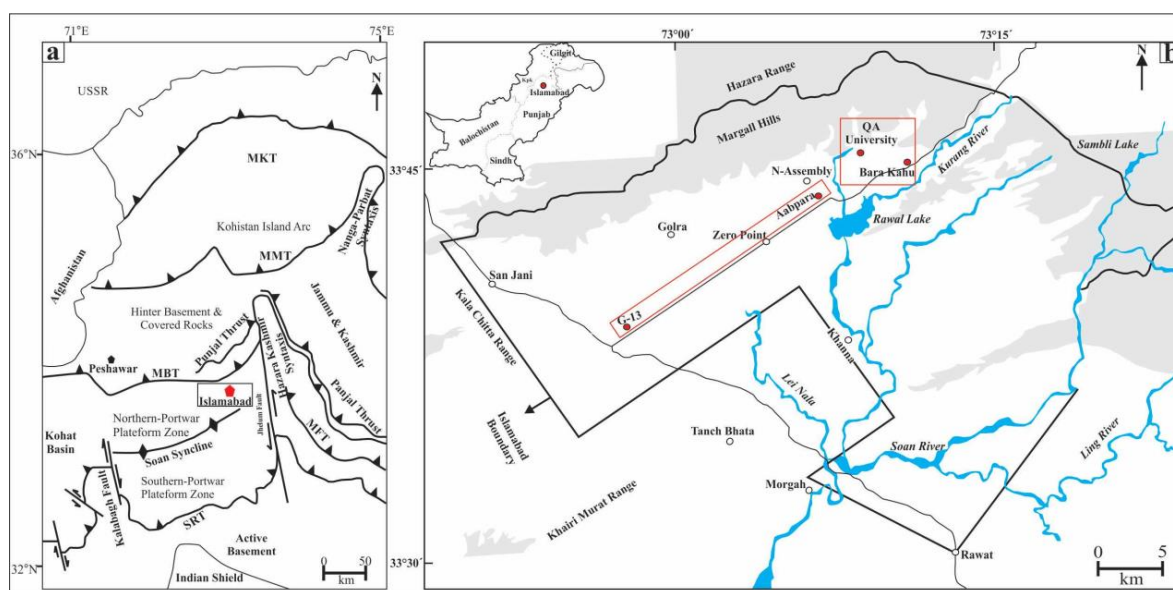

Figure 1. (**a**) Tectonic Model of Himalayan Fold and Thrust Belt, showing study area modified after [63]; Main Karakorum Thrust (MKT), Main Mantle Thrust (MMT), Main Boundary Thrust (MBT), Main Frontal Thrust (MFT), Salt Range Thrust (SRT) (**b**) Generalized map of Islamabad showing the site of investigations.

3. Methodology

The main focus of this research paper is to delineate aquifers using the 1D resistivity technique with 2D profiling adopting Schlumberger electrode configuration. A total of 23 vertical electrical soundings (VES) were conducted along six profiles (P-I, P-II, P-III, P-IV, P-I-G13, P-II-G13), with 13 VES executed in Area 1 and 10 VES in Area 2 (Figure 2). The Schlumberger array's depth of penetration is influenced by the spacing between current electrodes [69,70], resulting in the selection of VES locations for optimal coverage. The VES data acquisition involved the use of a TSQ-3 transmitter and RDC-10 receiver of Scintrex, powered by a generator accompanied by stainless steel electrodes and porous pot potential electrodes. Electrode configurations were optimized for maximum depth penetration, with potential electrode spacing (MN) ranging from 1 m to 50 m and current electrodes (AB) limited to 3 m to 1000 m [71]. The data acquired from the transmitter (I) and receiver (ΔV) are processed to calculate the apparent resistivity (ρ_a) (Equation (1)).
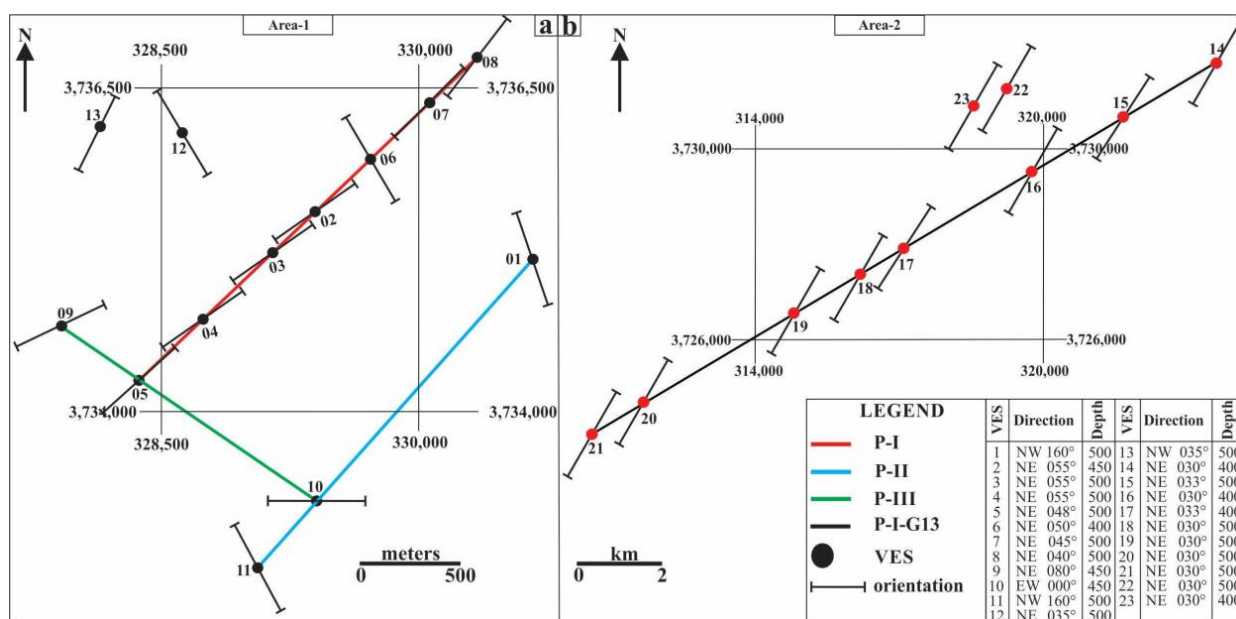

Figure 2. Base map of the study area, (**a**) Area 1 (Bara Kahu) showing orientation of VES with a total of 13 VES, (**b**) Area 2 (Aabpara to G13) showing stack of 10 VES.

The acquired VES data were modeled through curve fitting and inversion techniques to generate true resistivity profiles for each layer using the resistivity modeling software IPI2win [72]. Geoelectrical lithological sections (GELS) were prepared based on the resistivity values, showing lithological variations and delineating aquifer potential, thickness, depth, and type (confined and unconfined). Pseudosections were also created using inversion software (IPI2win) to visualize resistivity changes with depth along the collinear VES points. Statistical distribution curves of apparent resistivity were analyzed to examine the mean variation of resistivity and lithology along each profile. SDR (statistical distribution of resistivity) offers a comprehensive view of resistivity variations along each profile, providing insights through maximum, minimum, and mean resistivity values. This tool is highly valuable for interpreting the lithological distribution across various depths based on resistivity changes [32,73]. The data obtained from the borehole were additionally juxtaposed with the vertical electrical sounding (VES) data to assess their alignment and to determine the subsurface location and the condition of the aquifer in the vicinity.

Dar Zarrouk parameters such as total longitudinal conductance (S), longitudinal resistivity (ρ_L), transverse resistance (TR), and transverse resistivity (ρ_T) were calculated (Equations (2)–(6)). The Dar Zarrouk parameters of the study area are observed by taking account of acquired resistivity and its corresponding thickness. By analyzing these Dar Zarrouk parameters, researchers can gain insights into the subsurface's ability to transmit

fluids and obtain a better understanding of groundwater flow characteristics in the study area [31,74].

Kriging interpolation techniques were utilized to map the hydraulic parameters by incorporating the processed resistivity data. Surfer 10 software was used to create maps of aquifer thickness, depth, macroanisotropy, and true resistivity, providing insights into aquifer potential and lithological variations in the study area. The linear regression values (R^2) were calculated using statistical software (SPSS 16). The R^2 analysis examines the relationship between resistivity, depth, and thickness to understand the impact of these parameters on resistivity.

$$\rho = k(\Delta V/I) \tag{1}$$

$$k = \pi\,((AB/2)^2 - (MN/2)^2)/MN$$

where ρ is resistivity, ΔV is potential difference, and I is current

k is a geometric factor, MN (Potential electrode spacing), AB (Current electrode spacing), S (Total Longitudinal Conductance), h_1 (Layer 1 thickness), and H (Total Thickness)

$$\text{Total Longitudinal Conductance (S)} = \sum h_1/\rho_1 \text{ (mho)} \tag{2}$$

$$\text{Longitudinal resistivity } (\rho_L) = H/S \text{ } (\Omega m) \tag{3}$$

$$\text{Total transverse Resistance (TR)} = \sum \rho_1 \times h_1 \text{ } (\Omega m^2) \tag{4}$$

$$\text{Transverse Resistivity } (\rho_T) = TR/H \text{ } (\Omega m) \tag{5}$$

$$\text{Total Thickness (H)} = \sum h_{(1\ldots\cdot n)} \tag{6}$$

4. Results and Discussion

The IPI2win software was used to analyze the apparent resistivity (ρ_a) data by breaking it down into layers of true resistivity (ρ_T) with corresponding depth and thickness (Figures 3 and 4). The model curves of each VES are categorized into different geological units represented in the shape of a geoelectrical litho section with the basic concept of resistivity functional to lithology (Figure 5) [21,24,33,71,75]. The descriptive analysis of each VES is shown in Table 1.

Table 1. Descriptive analysis, hydraulic and lithological units of each VES.

VES	Resistivity		Std.Dev	Depth	Hydraulic Parameters					Lithological Units	Coordinates	
	Max	Min			S	T	A_S	A_T	Anisotropy		Easting	Northing
1	100	15	33	450	19	14,630	23	33	1.18	CS, SC, Sh, Sh-Cl	330,697	3,735,264
2	150	18	53	450	14	29,842	33	66	1.41	SC, Sh, St, Sh-Cl	329,700	3,735,325
3	55	08	19	500	50	6790	10	14	1.17	SC, Sh-Cl, Sa-Cl, Sh-Cl, Sh	329,260	3,735,124
4	200	15	74	500	23	14,180	22	28	1.14	SC, St, Sh, Sh-Cl	328,746	3,734,712
5	70	12	21	500	29	10,232	17	20	1.08	SC, Sh-Cl, CS, Sh-Cl, Sh	328,395	3,734,227
6	110	15	37	400	18	10,692	22	27	1.10	SC, Sh-Cl, Sh, CS	329,615	3,735,660
7	275	19	106	500	21	16,150	24	32	1.15	St, Sh-Cl, CS, Sh	329,970	3,736,390
8	60	15	16	500	25	14,180	20	28	1.18	CS, Sh-Cl, SC, Sh	330,352	3,736,757
9	280	22	120	450	19	15,540	24	35	1.20	St, Sh-Cl, Sh	327,910	3,734,700

Table 1. *Cont.*

| VES | Resistivity | | Std.Dev | Depth | Hydraulic Parameters | | | | | Lithological Units | Coordinates | |
	Max	Min			S	T	A_S	A_T	Anisotropy		Easting	Northing
10	80	24	20	450	10	20,984	43	47	1.04	Sa-Cl, Sh-Cl, Sa-Cl, Cl-Sa	329,356	3,733,353
11	62	32	12	500	13	19,528	37	39	1.02	Sa-Cl, St, Cl-Sa, Sh-Cl	329,070	3,732,787
12	225	42	84	500	11	24,350	46	49	1.03	St, Sa-Cl, Cl-Sa	328,620	3,736,160
13	60	13	20	500	22	12,641	23	25	1.05	Sa-Cl, Sh, Sh-Cl	328,156	3,736,201
14	106	15	37	400	15	14,446	27	36	1.15	Sa-Cl, Cl, Sa-Cl, Sh, Cl	323,753	3,731,831
15	414	40	159	500	12	27,340	43	55	1.13	St, Sa-Cl, Cl-Sa	321,340	3,730,350
16	105	11	43	400	29	10,494	14	26	1.39	Sa-Cl, Cl, Sa-Cl, Sh	319,815	3,729,440
17	200	8	75	400	30	24,204	13	61	2.14	Sa-Cl, Sh-Cl, Sh, St	317,230	3,727,875
18	250	15	107	500	13	78,750	39	158	2.01	Cl, Sh, St	316,216	3,727,269
19	102	14	32	500	13	22,699	39	45	1.08	Sa-Cl, Sh-Cl, Sh, Sa-Cl, Cl	314,960	3,726,400
20	260	13	92	500	14	84,759	37	170	2.14	Cl-Sa, Sh-Cl, Sa-Cl, Sh, St	311,739	3,724,669
21	300	20	101	500	10	88,400	49	177	1.90	Cl-Sa, Sa-Cl, Cl-Sa, Sh-Cl, St	310,567	3,724,016
22	300	4	119	500	23	112,670	21	225	3.25	Sa-Cl, Sh-Cl, Sh, St	319,055	3,731,160
23	100	10	39	450	41	6200	11	14	1.13	Sa-Cl, Cl, Sh	318,560	3,730,870
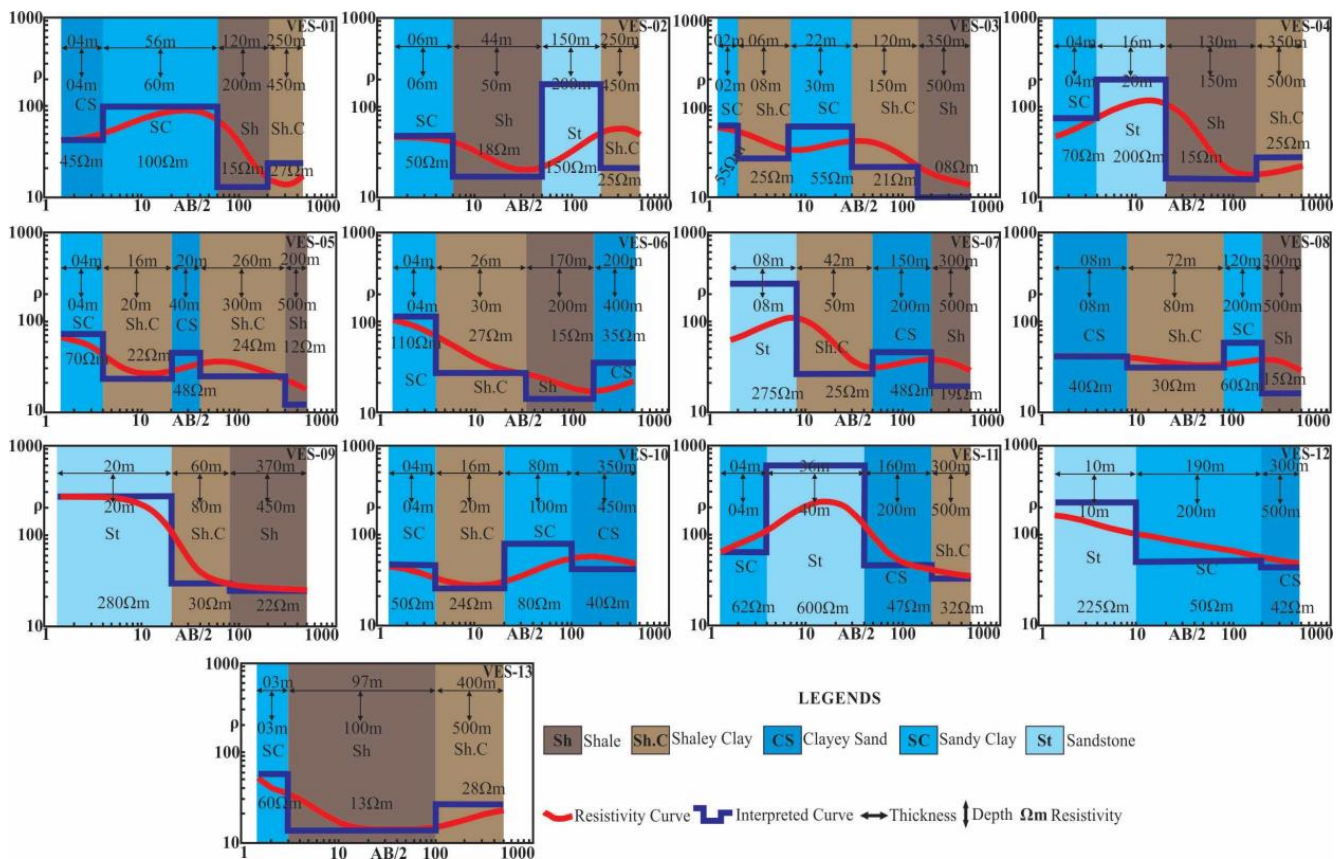
Figure 3. Geoelectrical sections of Area 1, portraying inverted resistivity curves divided into corresponding resistivity, depth, and thickness.
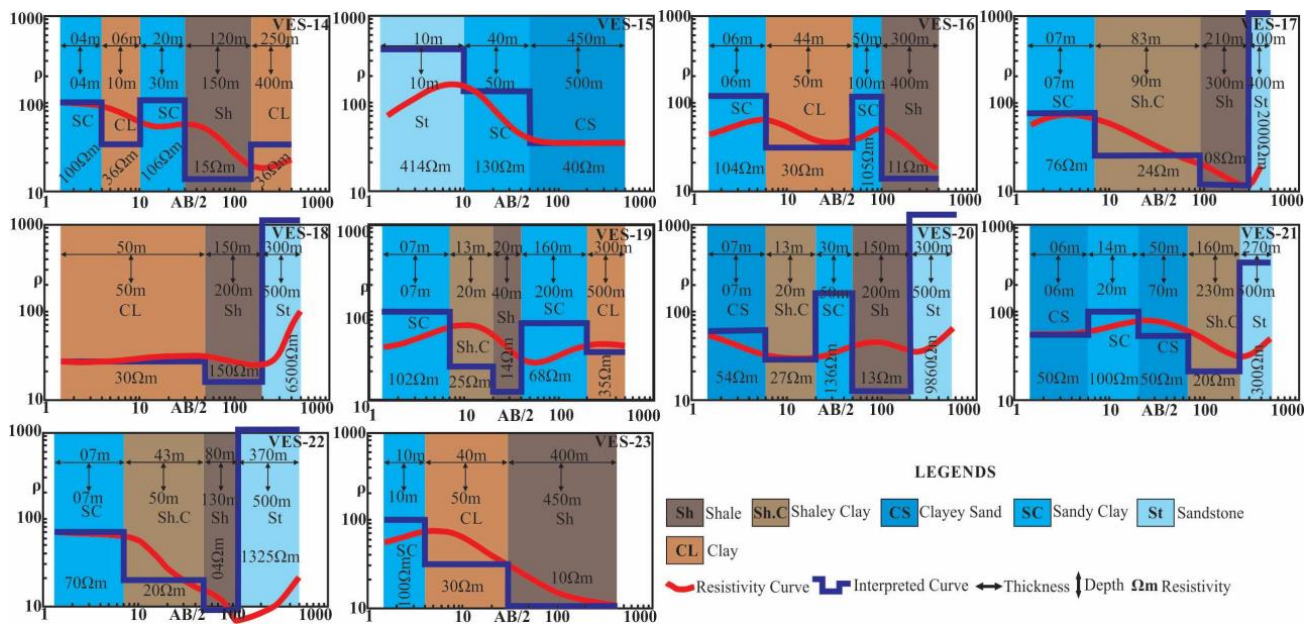
Figure 4. Geoelectrical sections of Area 2, portraying inverted resistivity curves divided into corresponding resistivity, depth, and thickness.
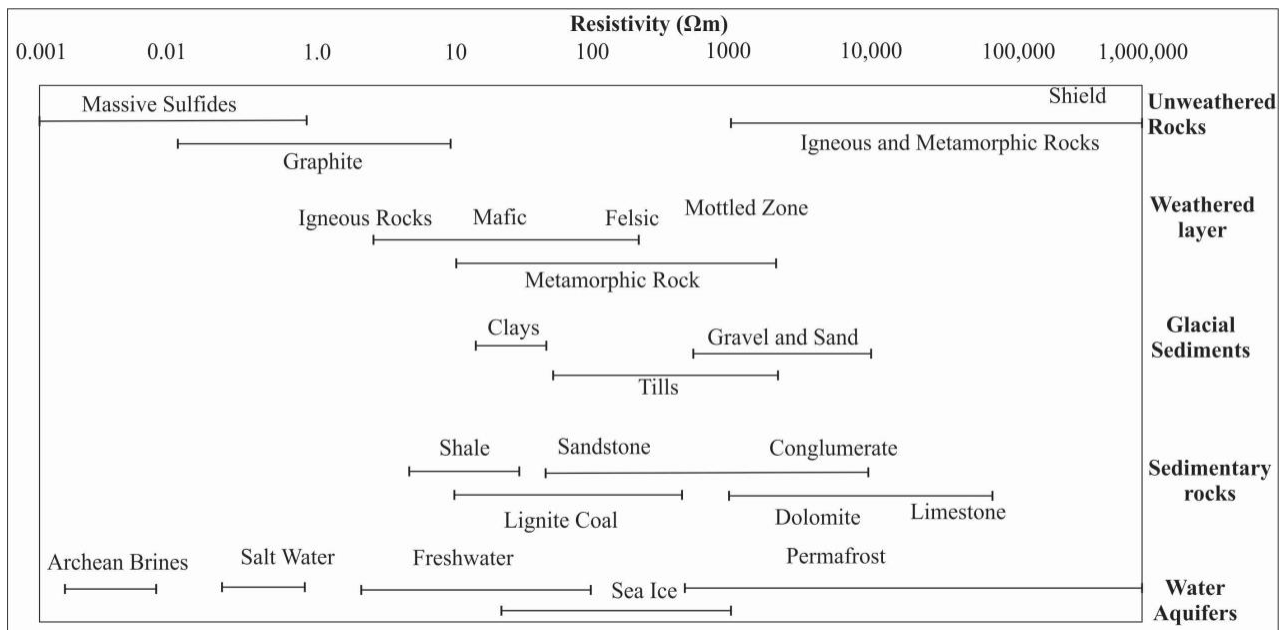

Figure 5. Resistivity Charts of different rocks and minerals displaying resistivity range [75].

4.1. Geoelectrical Litho Section (GELS)

GELS have been prepared for each VES to decipher the changing lithological fabrics and subsequent comparison with related VES along the profile to characterize aquifer prospects in desirable lithological units [32,66,73,76–78]. The IPI2win divides the VES field curves into different segments by adopting a curve fitting technique to signify changing resistivity shift vs. depth [72]. The differential resistivity is attributed to lithology assigning different resistivity values based on porosity, permeability, water chemistry, depth, and thickness of subsurface geological units [20–33]. A total of 23 GELS has been drawn showing different horizons to indicate aquifer potential having maximum probability of groundwater. The GELS for each VES are arrayed in six profiles showing depth, thickness,

and lithological accounts of discrete units. The GELS of study areas (1 and 2) unveil a total of six different lithological units predominantly of sandstone (150–600 Ωm), sandy clay (50–136 Ωm), clayey sand (35–54 Ωm), clay (30–36 Ωm), shaley clay (20–32 Ωm), and shale (04–22 Ωm) (Figures 3 and 4, Table 1). These lithological distributions interpreted from resistivity data align with the geology of the study area [62,64,65]. The prolific units for groundwater potential are sandstone, sandy clay, and clayey sand aided by an insignificant part of shaley clay. The resistivity range of 100 Ωm to 400 Ωm indicates the likely existence of a sandy lithological unit, which is a probable aquifer horizon as the unsaturated materials typically exhibit higher resistivity values [79]. Sandstone's high resistivity (VES-11, 600 Ωm) can be attributed to its compaction, cementation, and digenetic burial processes [80,81] (Figure 3). The high resistivity values, ranging from 1325 Ωm to 9860 Ωm, are interpreted as conglomeratic units (VES 17, 20, 22) (Figure 4). These conglomeratic units (Lie conglomerate) are in agreement with the geology of the area [62,65].

4.2. Geoelectrical Lithological Logs (GELL)

The GELL of each profiles P-I to P-IV (Area 1), and P-I-G13 to P-II-G13 (Area 2) were investigated using multiple collinear VES data. Each profile's lithological composition and aquifer potential were determined based on resistivity measurements vs. depth (Figures 6–8).
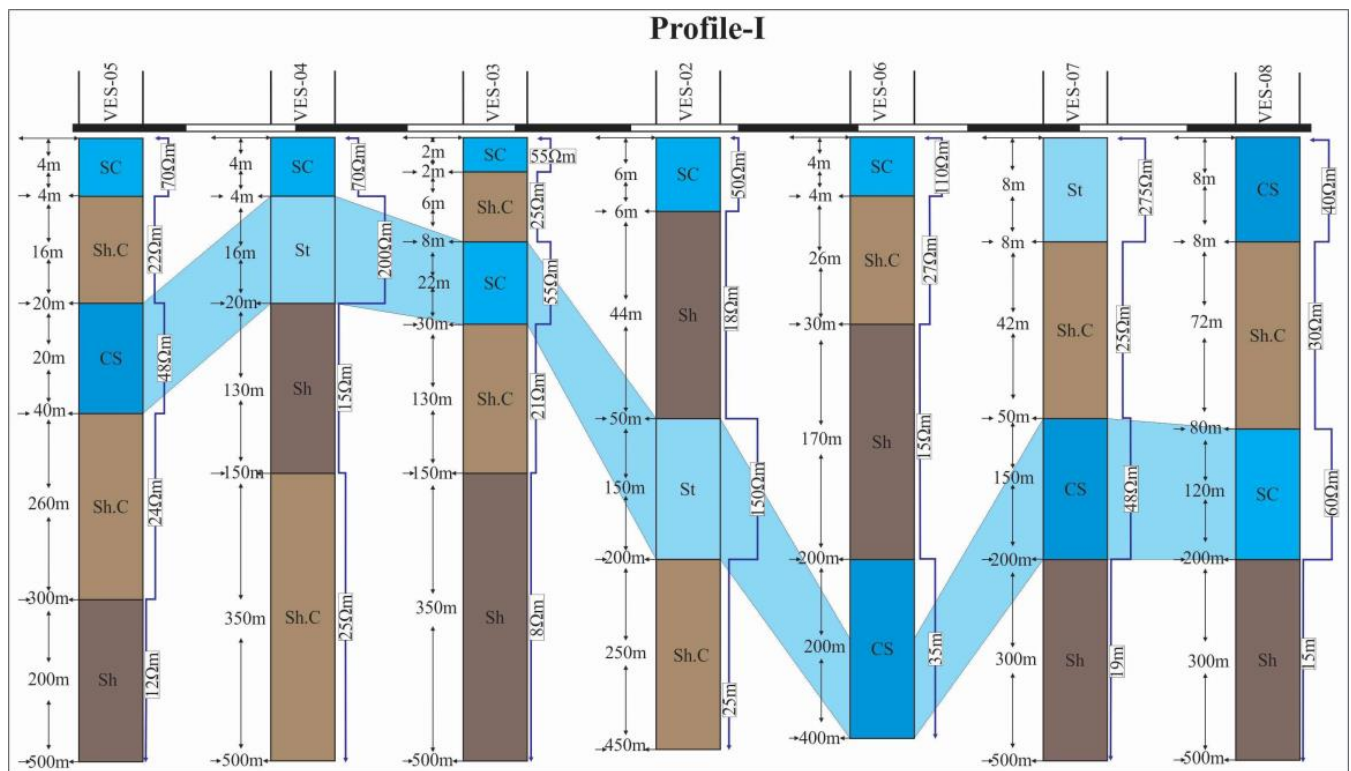

Figure 6. GELL of each VES arranged along P-I interpreted from resistivity data incorporating thickness and depth of each layer for aquifer potential delineation.
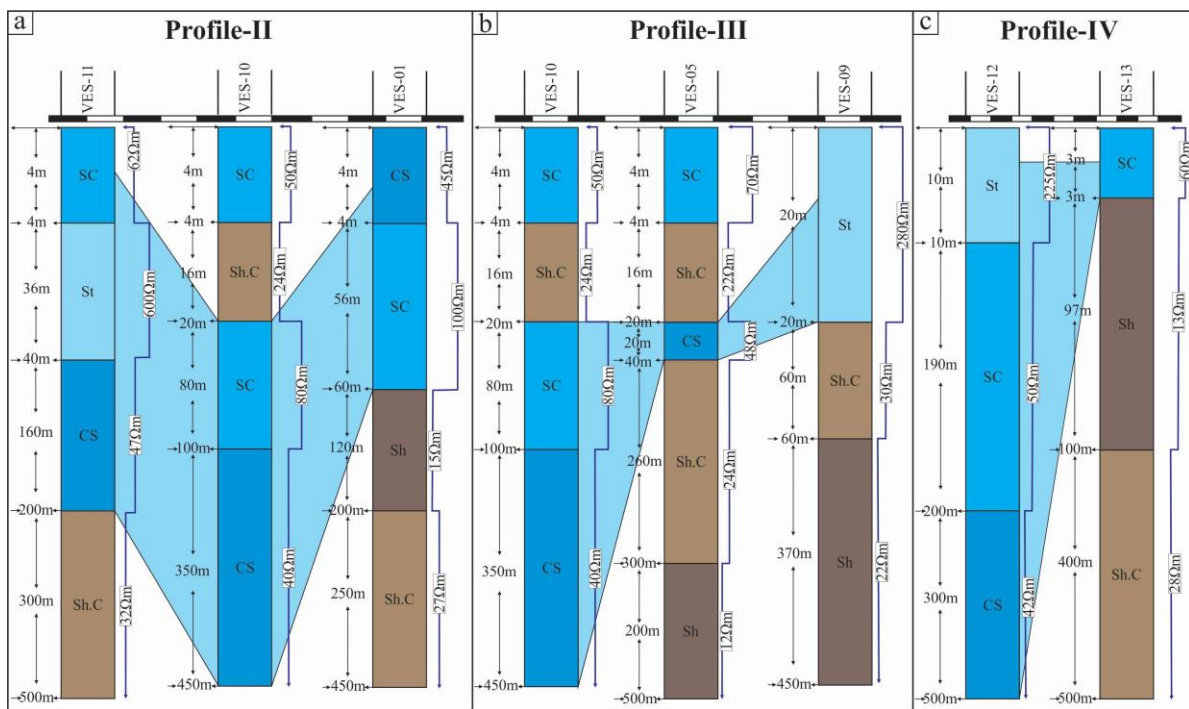
Figure 7. (**a**) GELL of P-II having a stack of three VES, (**b**) GELL of P-III having three VES demarcating shallow and deep aquifer horizons, (**c**) GELL of P-IV showing good aquifer potential along VES-12.
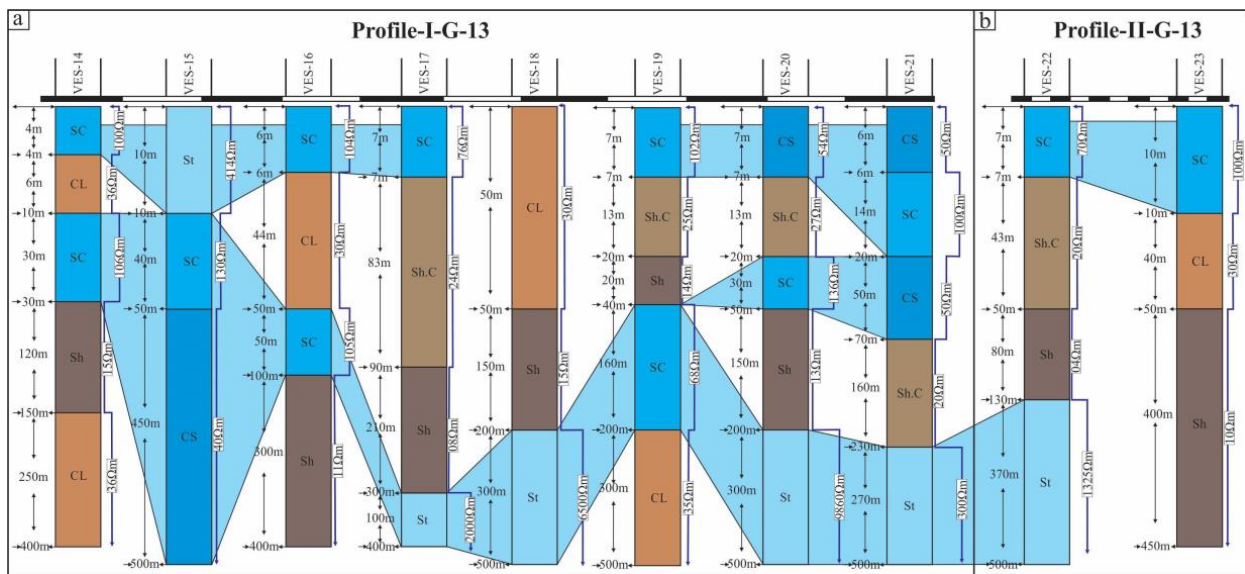

Figure 8. (**a**) GELL of P-I-G-13 positioned in Area 2 having a stack of 8 VES, demarcating shallow and deep aquifers, (**b**) GELL of P-II-G-13 showing aquifer potential.

Profile P-I, oriented NE–SW with a length of 3.2 km, exhibited sandy clay as the topsoil (4 m to 8 m depth, resistivity 40 Ωm to 70 Ωm), supporting shallow aquifers with good porosity. At greater depths, sandy content decreased, alternating with shaley clay (8 m to 40 m depth, resistivity 18 Ωm to 30 Ωm), forming confined horizons for underlying sandy units. Clayey sand (30 Ωm to 50 Ωm) and sandstone (270 Ωm to 280 Ωm) were identified as promising aquifers (40 m to 200 m depth) while shale (resistivity 8 Ωm to 15 Ωm) acted as confined beds for overlying sandy units (Figure 6). The shallow aquifers are delineated to a depth range of 8 m while deeper aquifers are at depth ranges more than 20 m.

Profile P-II, oriented NW–SE with a length of 2 km, and was dominated by sandy clay and clayey sand, with minor amounts of shaley clay and shale. The top sandy clay (50 Ωm to 62 Ωm) merged into clayey sand (100 m depth). Shaley clay and clay dominated at different depths, and sandstone (250 Ωm to 300 Ωm) constituted semi-confined aquifers (Figure 7). Profile P-III, with a length of 3 km and oriented NW–SE, was characterized by descending layers of shaley clay, sandy clay, clayey sand, shale, and sandstone. Shallow aquifers were found in sandy clay and sandstone beds (10 m to 200 m depth), while shaley clay acted as confining layers (Figure 7). Profile P-IV, spanning 500 m in the E–W direction, showed promising aquifer potential in sandy clay/sandstone layers (10 m to 200 m depth), while the presence of shale and clay indicated limited potential (Figure 7).

Profile P-I-G13, spanning 16.5 km from Aabpara to G-13, exhibited multiple lithological units, with sandy clay, clayey sand, and sandstone presenting the highest groundwater potential. Sandy clay served as shallow aquifers (10 m to 50 m depth), and sandstone formed deeper aquifers (over 200 m depth) (Figure 8). Profile P-II-G13, 2 km in length, featured sandy clay (7 m depth) at the surface, followed by shaley clay, shale, and clay layers (up to 500 m depth), with deeper and confined aquifers present in sandstone beds (120 m depth) (Figure 8).

The GELL is compared with the borehole data, which shows agreement with the lithological distribution and aquifer distribution [62]. The aquifer horizons are mostly sandstone, gravel, and sand, the same as the GELL, where the aquifer horizons are sandy clay, clayey sand, and sandstone (Figure 9). The aquifers are shallow surficial aquifers with a depth range of 11 ft to 61 ft (Figure 9); these shallow aquifers are prone to contamination [44,45,48]. The deeper aquifers, located at depths exceeding 50 m and confined within sandy lithological units, represent the potential source horizon for high-quality water, as determined by the resistivity survey.
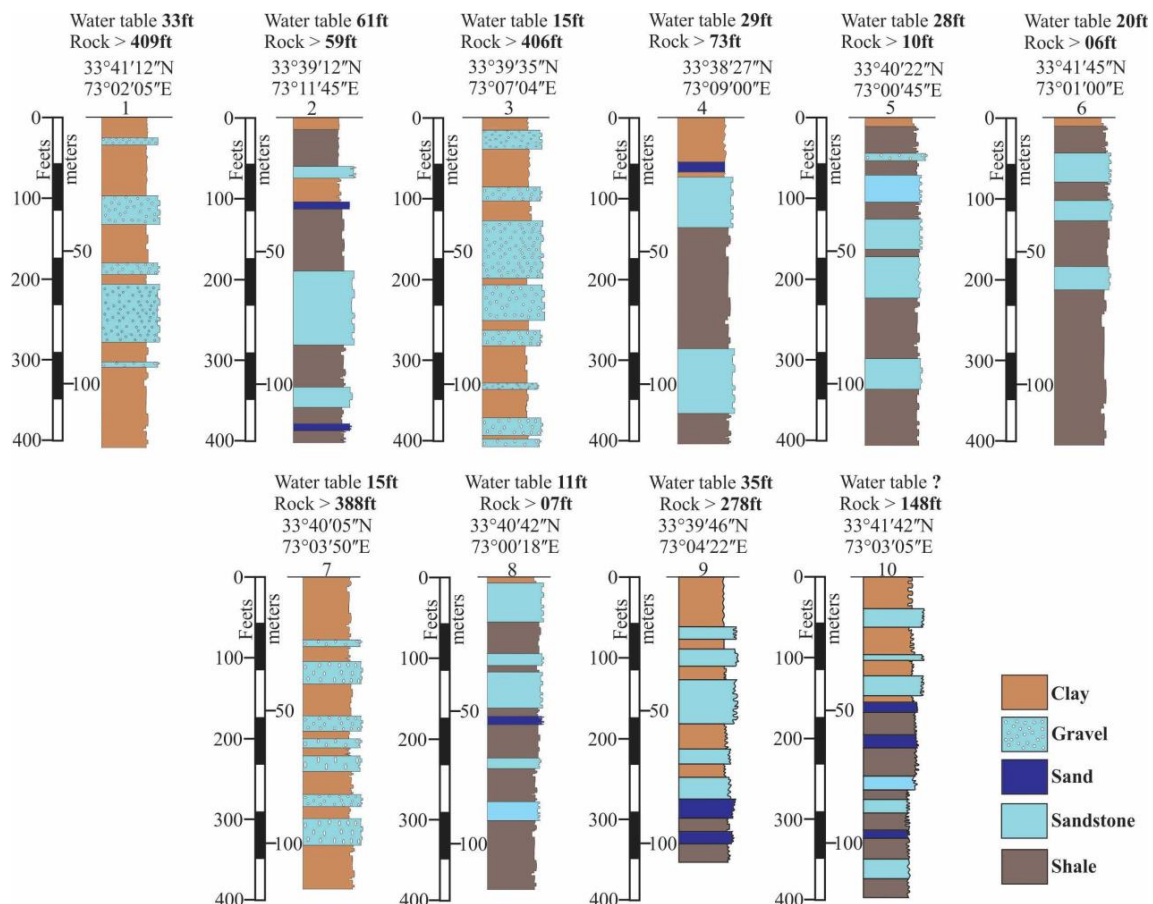

Figure 9. Borehole logs around Islamabad by the Capital Development Authority [62].

4.3. Pseudosection of Apparent Resistivity

The pseudosection (PS) technique was applied to portray the overall resistivity trend along each profile (P-I to P-III and P-I-G13). The PS combines and correlates resistivity values from multiple collinear VES to decode the distribution of lithological units along the profiles. However, PS for P-IV and P-II-G13 could not be generated due to the presence of fewer than three collinear VES, so their aquifer potential was delineated from GELS data along the sections (Figure 10).
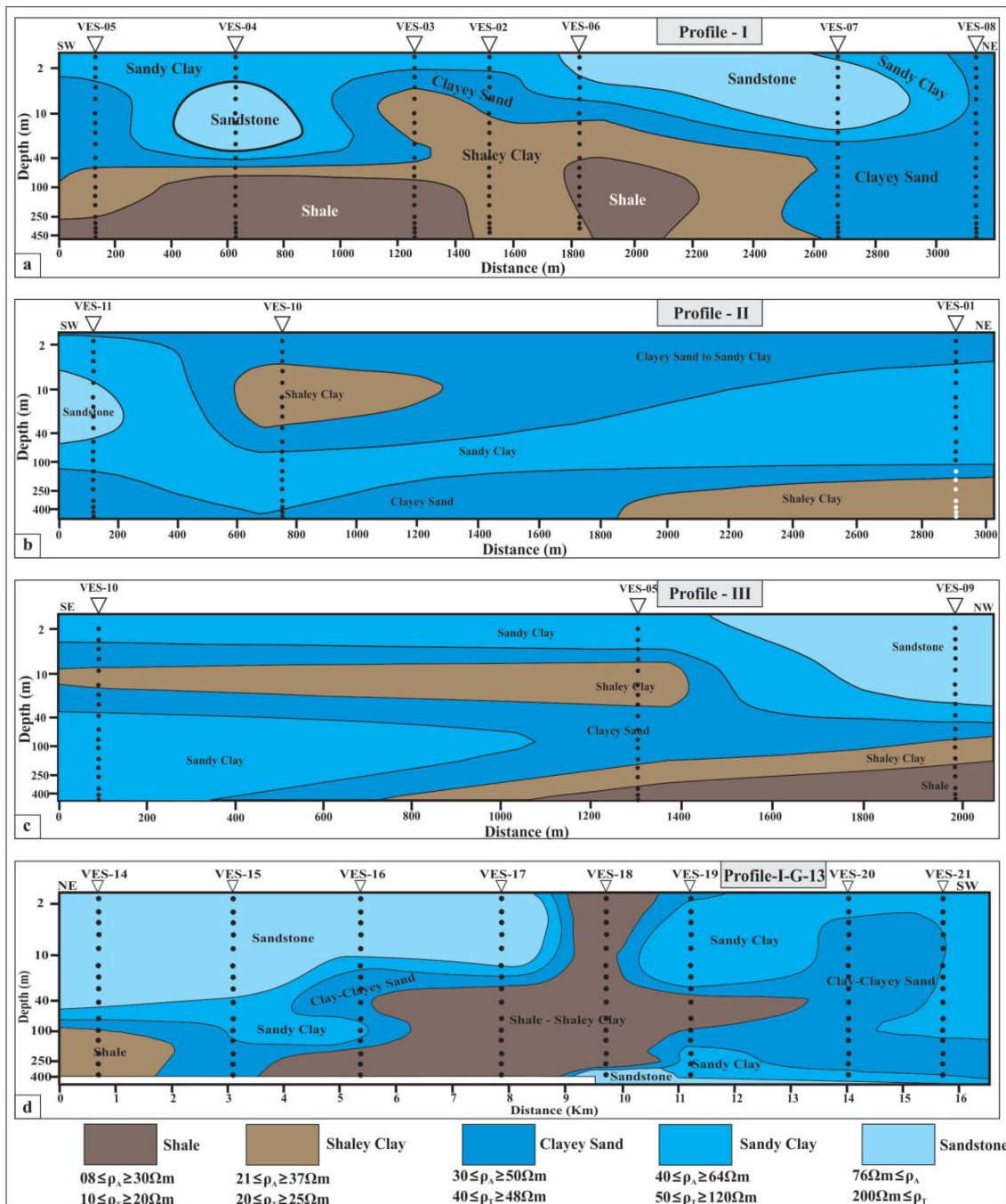

Figure 10. Pseudosection of Area 1 and 2, (**a**) PS of P-I sandy clay to sandstone with depth fine content increases, (**b**) PS of P-II displaying clayey sand to sandy clay alternating with clayey sand and shaley clay, (**c**) PS of P-III represent sandy clay alternating with clayey sand and finer with depth along NW side, (**d**) PS of P-I-G13 sandstone and sandy clay with different lithological units along NE and SW side.

The PS-P-I revealed that there is a change in lithology in a steady way with depth; the topsoil is mostly sandy, and with an increase in depth, clay dominates downward reaching clayey sand, shaley clay, and shale (Figure 10a). The lensoidal sandstone beds are encountered by VES-04, 06, and 07 with a depth of $\geq$1.5–$\geq$4 m and a resistivity (apparent and true) of $\geq$85–$\leq$110 Ωm and $\geq$200–$\leq$275 Ωm. The aquifer potential includes shallow beds of sandy clay ($\geq$40–$\leq$57 Ωm and $\geq$46–$\leq$110 Ωm) at a depth of $\geq$2–$\leq$30 m. The deeper aquifers are shown by clayey sand ($\geq$30–$\leq$38 Ωm and $\geq$32–$\leq$48 Ωm) with a depth of $\geq$30–$\leq$100 m attributed to an increase in thickness along the NE side. The deeper lithologies are predominantly shale ($\geq$08–$\leq$18 Ωm and $\geq$08–$\leq$22 Ωm) and shaley clay ($\geq$21–$\leq$33 Ωm and $\geq$20–$\leq$30 Ωm), having a depth of >100–$\leq$500 m, with pronounced depth at the NE side. The sandy clay sustains shallow aquifers through good porosity and permeability of the clayey part and permeability of the sand portion, making a good reservoir [44,79–81]. The pseudosection is in agreement with the geologs in deciphering the same lithology after inversion.

PS of P-II disclosed the presence of clayey sand ($\geq$30–$\leq$38 Ωm and $\geq$39–$\leq$50 Ωm) to sandy clay ($\geq$45–$\leq$64 Ωm and $\geq$45–$\leq$80 Ωm) as surface lithology with $\geq$1.5–$\leq$100 m depth with an increase in thickness along VES-10 (Figure 10b). The sandy content increases downward, leading to sandy clay with maximum thickness shown by VES-11 and 01. The shaley clay is also pictured by VES-01 and 10 as a pinch out of beds at depths of 04 m and 250 m, respectively. The best aquifer horizon is present in the form of sandy clay having a depth of $\geq$15–$\leq$100 m for VES-11, $\geq$60–$\leq$400 m for VES-10, and $\geq$10–$\leq$200 m for VES-01. The shallow aquifers are present in the form of clayey sand with an average depth of $\geq$1.5–$\leq$60 m. The aquifers present there are mostly unconfined having maximum discharge and recharge due to the presence of a considerable amount of sand [23,80,81].

The PS of P-III pseudosection pictured sandy clay ($\geq$52–$\leq$56 Ωm and $\geq$50–$\leq$70 Ωm) and sandstone ($\geq$242 Ωm) as surface lithology exhibiting a depth of $\leq$20 m, dominated by sandstone at the NW side (Figure 10c). The clayey content increases with depth and is pictured as shaley clay ($\geq$25–$\leq$31 Ωm and $\geq$22–$\leq$30 Ωm) as pinch-out beds at a depth of $\geq$10–$\leq$20 m in clayey sand ($\geq$30–$\leq$50 Ωm and $\geq$40–$\leq$48 Ωm). At greater depth, the lithological units are delineated by maximum sandstone at the SE side, while on the NW side, shaley clay to shale ($\geq$18–$\leq$24 Ωm and $\geq$12 Ω–$\leq$22 Ωm) dominates. The aquifer horizon is sandy clay and clayey sand having a depth of $\geq$05 m, bounded by shaley clay at the base making it a semi-confined aquifer. The thickness of aquifer beds decreases toward the NW side, with good water potential along the VES-10 at 40 m by sandy clay units. The VES-05 generates a confined aquifer capped by shaley clay, while in VES-09 and 10, the aquifers are mostly semi-confined.

The PS of P-I-G13 elaborates an alternating sequence of lithological units with clear distinction in the NE and SW sides marked by a probable shear zone of shale–shaley clay ($\geq$15–$\leq$25 ΩmρA and $\geq$05–$\leq$20 ΩmρT) (Figure 10d). The NE side has sandy units of sandstone ($\geq$70–$\leq$90 ΩmρA and $\geq$300–$\leq$650 ΩmρT), sandy clay ($\geq$50–<70 ΩmρA and $\geq$150–<300 ΩmρT), and clayey sand ($\geq$40–<50 ΩmρA and $\geq$100–<150 ΩmρT), clay ($\geq$30–<40 ΩmρA and $\geq$50–< 100 ΩmρT) and shale (<15 ΩmρA and <20 ΩmρT) at greater depth, while the SW side is dominated by sandy clay, clayey sand, clay, and sandstone. The pseudosection revealed area has very good aquifer potential in sandstone and sandy clay, with a promising depth of $\geq$10–$\leq$40 m. The results are in agreement with the geology of the area and borehole litho section [62,64,65]. With the increase in depth, the NE side is dominated by clay, while on the SW side sandstone dominates.

4.4. Statistical Distribution of Resistivity

SDR (statistical distribution of resistivity) plots are created for identical pseudosection profiles to illustrate the average resistivity changes with depth. These plots also indicate the occurrence of different lithologies at regular intervals, along with the probability of water content [32,66,73,78]. Each profile's SDR data are analyzed using IPI2win to calculate the mean statistical variation of resistivity (Figure 11).
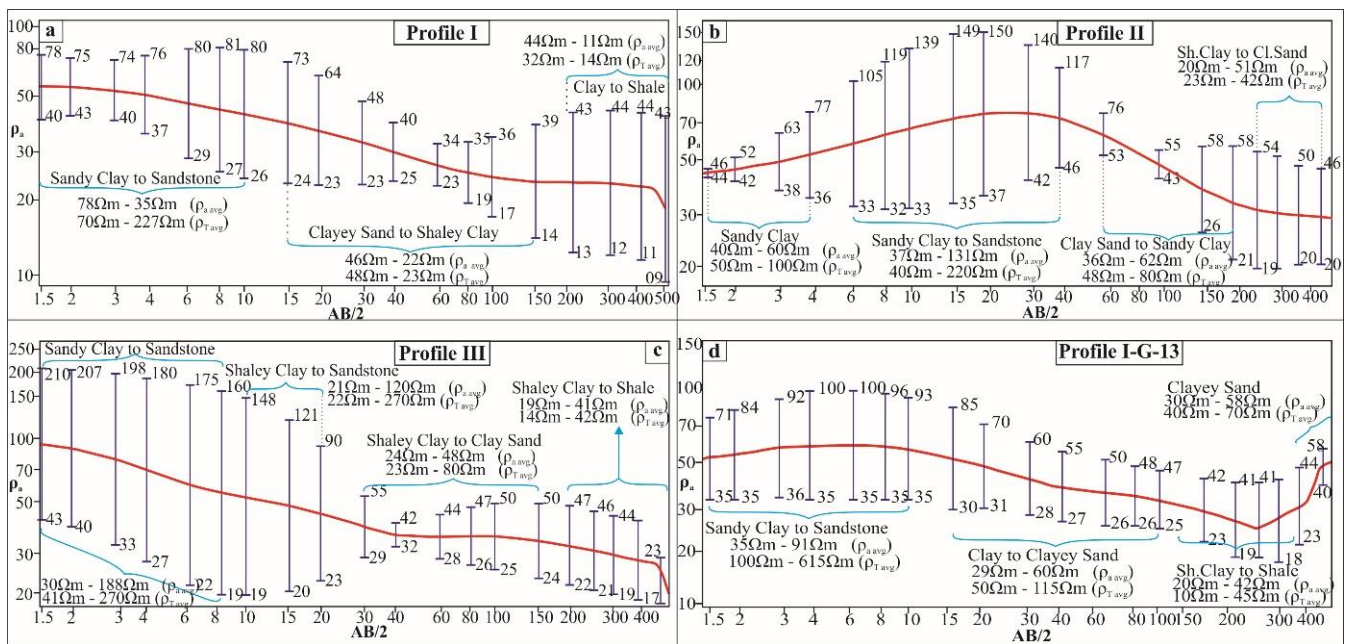
Figure 11. (**a**) SDR of P-I displaying gentle downward trend leading from sandy to shaley units, (**b**) SDR of P-II showing gentle rise and fall leading from sandy clay to shaley clay, (**c**) SDR of P-III showing steep drop from sandstone to shale, (**d**) SDR of P-I-G-13, a subtle drop and steep rise at depth showing differentiating lithologies.

The SDR analysis of Profile P-I reveals a distinct lithological sequence, with the upper horizon ranging from sandy clay to sandstone. The average apparent resistivity (ρ_{aavg}) and average true resistivity (ρ_{Tavg}) values vary within specific ranges for each lithology. The transition from sandy clay to sandstone occurs gradually, with an average resistivity change of 43 Ωm, corresponding to a 135% increase and a 55% decrease. Specifically, the sandy clay experiences an average increase of 36 Ωm (90% increase, 47% decrease), while the sandstone shows a rise of 53 Ωm (195% increase, 67% decrease). As we go deeper from 10 m to 150 m, the lithologies shift to clayey sand and eventually to shaley clay. The resistivity values for this sequence range from $\rho_{aavg} \geq 22$ Ωm to ≤ 46 Ωm and $\rho_{Tavg} \geq 23$ Ωm to ≤ 48 Ωm. The average resistivity increase from clayey sand to shaley clay is 26 Ωm, with a 122% increase and a 52% decrease. Clayey sand itself experiences an average increase of 33 Ωm (138% increase, 55% decrease) in the depth range of ≥ 10 m to ≤ 40 m. For shaley clay, the resistivity increases by 18 Ωm (106% increase, 49% decrease) as we go deeper from >40 m to ≤ 150 m. At depths greater than 150 m, lithologies like clay and shale are encountered, characterized by resistivity values ranging from $\rho_{aavg} \geq 11$ Ωm to ≤ 44 Ωm and $\rho_{Tavg} \geq 14$ Ωm to ≤ 32 Ωm. The average resistivity increase for this sequence is 33 Ωm, with a 300% increase and a 75% decrease from clay to shale. The primary trend observed in the SDR analysis of P-I is a gradual shift in lithologies, indicating changes in the depositional environment with decreasing sand content down the sequence. Deeper marine sequences are encountered as we go further down, leading to finer clayey and shaley facies. The most promising reservoir rocks are found in sandstone and clayey sand units at depths of >4 m to ≤ 40 m. The significant percent increase in resistivity for the sandy unit (138%) is attributed to the presence of water content, which elevates the resistivity values. The resistivity values of clayey sand also show fluctuations, with an increase from 48 Ωm to 56 Ωm (an 8 Ωm shift) due to water content, and a decrease from 30 Ωm to 25 Ωm (a 5 Ωm shift) representing a sandier content, indicative of a good probable horizon. The permeable cap rocks, sandy clay, and sandstone play a crucial role in recharging the underlying aquifer. However, the shaley and clayey beds at the base act

as barriers, limiting downward recharge and leading to the presence of shallow aquifer beds with good potential for potable water (Figure 11a).

The SDR analysis of Profile P-II reveals a distinctive lithological sequence, starting with sandy clay and transitioning to sandstone units in a gentle upward trend. However, at a deeper level (as shown in Figure 11b), there is a sharp decrease in resistivity, indicating the presence of clayey sand, sandy clay, and shaley clay. In the topsoil layers, which extend to a depth of $\leq$4 m, the dominant lithology is sandy clay, characterized by resistivity values ranging from ρaavg $\geq$ 40 Ωm to $\leq$60 Ωm and ρTavg $\geq$ 50 Ωm to $\leq$100 Ωm. These layers are favorable for good recharge. The average resistivity increase for this section is 20 Ωm, with a percent increase of 52% and a decrease of 29%. As we go deeper from >4 m to $\leq$40 m, the lithologies change from sandy clay to sandstone, with ρaavg and ρTavg values ranging from $\geq$37 Ωm to $\leq$131 Ωm and $\geq$40 Ωm to $\leq$ 220 Ωm, respectively. The resistivity trend shows a gentle upward shift with increasing sand content, leading toward sandstone from sandy clay. The average resistivity increase for this transition is 94 Ωm, indicating a total change of 74 Ωm and a percent increase of 307%, which suggests a steeper change due to a significant input of sandy materials replacing clayey content. The average percent increase and decrease are 261% and 72%, resulting in a total percent increase of 209% and a decrease of 43% from the sandy clay layer. At depths from >40 m to $\leq$200 m, there is a steep drop in resistivity, signifying the change from sandstone to clayey sand. The ρ_{aavg} and ρ_{Tavg} values for this clayey sand layer range from $\geq$36 Ωm to $\leq$62 Ωm and $\geq$48 Ωm to $\leq$80 Ωm, respectively. The average resistivity increase and decrease for the clayey sandstone layer are 26 Ωm and 68 Ωm, with a percent decrease of 72% from the overlying sandstone bed. The total percent increase and decrease in resistivity are 94% and 43%, with a total percent decrease of 167% and an increase of 29% from the sandstone layer. The steep drop in resistivity is attributed to the presence of clayey beds with sand, aided by compaction and the existence of water content in pore spaces [79–81]. At a depth of > 200 m, the sandy content of the sandy clay decreases due to the input of fines, leading to the formation of shaley clay and clayey sand layers [29,82]. The resistivity window for this horizon ranges from $\rho_{aavg} \geq$ 20 Ωm to $\leq$51 Ωm and $\rho_{Tavg} \geq$ 23 Ωm to $\leq$42 Ωm. The average resistivity increase for this transition is 31 Ωm, with a percent increase of 158% and a decrease of 61%. The resistivity rise from the overlying clayey sand is 5 Ωm, with a percent increase of 64% and a drop of 18%. The minimal rise from the overlying horizon is attributed to the presence of mixed lithologies, including shale and sand, with maximum compression of overlying materials and less porosity [49,56,62,80,81].

The SDR analysis of Profile P-III shows distinct lithological changes. At the surface, from a depth of $\geq$1.5 m to $\leq$8 m, there is a steep drop in resistivity due to the presence of sandy clay to sandstone, with resistivity values ranging from $\geq$30 Ωm to $\leq$188 Ωm (ρ_{aavg}) and $\geq$41 Ωm to $\leq$270 Ωm (ρ_{Tavg}). The average resistivity change is 158 Ωm, with a significant percent increase of 552% and a decrease of 83%. This drop in resistivity is mainly caused by surficial water and the mixing of clay with sandstone, facilitated by loose compaction [28,29,31,82]. As we go deeper, at depths of >8 m to $\leq$20 m, there is a mixing of shale with sandstone, forming shaley clay. The resistivity for this section ranges from $\geq$21 Ωm to $\leq$120 Ωm (ρ_{aavg}) and $\geq$22 Ωm to $\leq$270 Ωm (ρ_{Tavg}). The average resistivity increase is 99 Ωm, with a percent change of 492% (increase) and 81% (decrease). The resistivity shift from overlying sandy beds is 59 Ωm, with a percent decrease of 60% and an increase of 2%. This resistivity change is attributed to the presence of shaley content, along with the influence of clay [26,35]. At greater depths, from >20 m to $\leq$150 m, shaley clay and clayey sand are encountered, with resistivity values ranging from $\geq$24 Ωm to $\leq$48 Ωm (ρ_{aavg}) and $\geq$23 Ωm to $\leq$80 Ωm (ρ_{Tavg}). The average resistivity increase is 31 Ωm, with a percent increase of 68% and a decrease of 42%. The resistivity shift from overlying sandstone is 68 Ωm, with a percent decrease of 424% and an increase of 39%. This steep and abrupt change occurs as sandstone disappears and is replaced by clayey sand, which is also influenced by the presence of water content [83]. The last horizon, at a depth range of >150 m, represents shaley clay and shale, with resistivity values of $\geq$19 Ωm to $\leq$41 Ωm

(ρ_{aavg}) and $\geq$14 Ωm to $\leq$42 Ωm (ρTavg). The average resistivity increase is 25 Ωm, with a percent increase of 139% and a decrease of 56%. The drop in resistivity from overlying beds is 6 Ωm, with a percent decrease of 19%. The SDR analysis of P-III reveals the presence of favorable shallow permeable beds consisting of sandy clay and sandstone at a depth range of $\geq$5 m to $\leq$20 m. These lithologies serve as excellent cap rocks, promoting the recharge of the underlying clayey sand aquifer, which extends from >20 m to $\leq$150 m with a thickness of 120 m. Below this aquifer, there are impermeable layers composed of shaley clay and shale. The aquifer from Profile P-II is semi-confined at its base, indicating a significant water potential for long-term water supply and recharge (see Figure 11c).

The SDR analysis of P-I-G13 (Area 2) indicates a gradual decline in resistivity down to a depth of 250 m, followed by a sudden and steep rise (Figure 11d). The topsoil is primarily composed of sandy clay to sandstone, ranging from $\geq$1.5 m to $\leq$10 m in depth, with resistivity values of $\geq$35 Ωm to $\leq$91 Ωm (ρ_{aavg}) and $\geq$100 Ωm to $\leq$615 Ωm (ρ_{Tavg}). The average resistivity increase for this top horizon is 159%, with a decrease of 61%, resulting in a total fluctuation of 90 Ωm and 57 Ωm. As we go deeper, from >10 m to $\leq$100 m, the resistivity decreases, indicating the presence of clay to clayey sand lithology, with values ranging from $\geq$29 Ωm to $\leq$60 Ωm (ρ_{aavg}) and $\geq$50 Ωm to $\leq$115 Ωm (ρ_{Tavg}). The average resistivity increase is 31 Ωm, with a percent increase of 111% and a decrease of 52%. The resistivity drops by 32 Ωm from overlying sandstone, representing a percent decrease of 35%. From >100 m to $\leq$ 350 m, the dominant lithologies are shaley clay and shale, with resistivity values of $\geq$10 Ωm to $\leq$42 Ωm (ρ_{aavg}) and $\geq$20 Ωm to $\leq$ 45 Ωm (ρ_{Tavg}). The average resistivity increase is 22 Ωm, with a percent increase of 112% and a decrease of 53%. The resistivity decreases by an average of 17 Ωm from overlying clayey sand, indicating a decrease of 29%. At depths beyond > 350 m, the prevailing lithology is clayey sand, with resistivity ranging from $\geq$30 Ωm to $\leq$58 Ωm (ρ_{aavg}) and $\geq$40 Ωm to $\leq$70 Ωm (ρ_{Tavg}). The average resistivity increase is 22 Ωm, with a percent increase of 74% and a decrease of 41%. There is an average increase of 15 Ωm from overlying shale, representing a percent increase of 36%. The SDR analysis deduced that the area has good potential reservoirs, particularly within a depth range of $\geq$10 m to $\leq$100 m. The cap rock is predominantly sandy, and as the depth increases, the clayey content becomes more prevalent, typically after an average depth of 250 m. The steep increase in resistivity is indicative of the lithological units and supports the presence of a fault zone or conglomeratic lithologies in the P-I-G-13 pseudosection [63–65,84].

4.5. Dr Zarrouk of Hydraulic Parameters
4.5.1. Area 1

In study Area 1, the longitudinal unit conductance (S) fluctuates between $\geq$10 mho and $\leq$50 mho, showing the aquifer's potential to hold water, directly related to its porosity. The highest S value is concentrated in the SW, centered at VES-03 with a value of 50 mho (Figure 12a). Conversely, S decreases systematically along the NW and SE periphery, with the lowest values observed at VES-12, 11, 10, 06, and 02.

On the other hand, the longitudinal resistivity (ρ_L) follows a reverse trend compared to S, ranging from $\geq$10 Ωm to $\leq$43 Ωm (Figure 12b). Maximum resistivity is observed at the SE and NW regions, specifically at VES-12, 11, and 10. The lowest ρ_L value is recorded at the center of the SW side, with a value of 10 Ωm at VES-03, 04, and 05. From S and ρ_L values, it is inferred that the area has good porous lithology of clay and shale along VES-05, 04, and 03 [85–87]. The presence of sandstone enhances resistivity due to its compact nature and water content, resulting in maximum ρ_L values on the SE and NW sides [87]. The total transverse resistance (TR), directly related to water transmission ability and permeability, ranges from 6000 Ωm^2 to 38,000 Ωm^2 in study area 1 (Figure 12c). Lower TR values are found in the SW and center, particularly along VES-06, 05, 04, and 03, while higher values are recorded along the SE and NW sides, specifically at VES-10, 11, and 12. The transverse resistivity (ρT) follows a similar trend to TR, ranging from $\geq$10 Ωm to $\leq$80 Ωm (Figure 12d). Minimum ρT values are observed at VES-05, 04, 03, and 06, ranging from $\geq$10 Ωm to

≤25 Ωm in the SW to the center. The maximum ρT values of 60 Ωm to 80 Ωm are observed at VES-12, 11, and 10 in the SE and NW regions of the study area. These results indicate that the SW and central part of the study area contain impermeable beds of clays, while the SE and NW regions consist of good porous beds of sandstone, showing potential sites for aquifers [87]. The macro-anisotropy, derived from longitudinal conductance and transverse resistance data, reveals lithological changes related to hydraulic parameters [88]. The macroanisotropy map with values ranging from ≥1.02 to ≤1.38 (Figure 13a) is consistent with the true resistivity map. Lower macroanisotropy values (≥1.02 to ≤1.11) are confined to the SE to NW zone, while higher values (≥1.29 to ≤1.38) are observed at the SW and NE sides of the study area. The NW side exhibits good aquifer potential according to macroanisotropy. Overall, the NE and SE sides are inferred to have good aquifer potential probability based on macroanisotropy. A true resistivity section was created to portray the resistivity distribution in the study area, ranging from ≥25 Ωm to ≤280 Ωm (Figure 13b). The section illustrates the distribution of minimum and maximum resistivity values and the presence of distinct lithological units. Lower resistivity (≥25 Ωm to ≤70 Ωm) is found in the SE–SW side, gradually increasing toward the NE and NW. The resistivity divide is marked by SSW and NNE trending lines with resistivity values ranging from ≥60 Ωm to ≤80 Ωm. The higher resistivity values (≥200 Ωm to ≤280 Ωm) are recorded in the NSW and NNE side of the study Area 1. The overall trend of true resistivity suggests that the NE and NW sides contain maximum sandstone to sandy clay, while the SE and NE sides are dominated by clayey sand to shale [21,57,71,79].

4.5.2. Area 2

In Area 2, the longitudinal conductance (S) shows a symmetrical increase from the SW and NE sides toward the center, ranging from ≥10 mho to ≤40 mho (Figure 14a). VES-22, 23, 17, and 16 exhibit the highest values (≥30 mho to ≤40 mho), while VES-14, 15, 18, 19, and 20 shows the lowest values (≥10 mho to ≤15 mho). In contrast, the longitudinal resistivity (ρ$_L$) follows an opposite trend, ranging from ≥10 Ωm to ≤50 Ωm, decreasing from the NE–SW side toward the center (Figure 14b). VES-14, 15, 18, 19, 20, and 21 have the highest ρ$_L$ values (≥35 Ωm to ≤50 Ωm), while VES-17, 18, 22, and 23 exhibits the lowest values (≥10 Ωm to ≤18 Ωm). These findings indicate that the center of the area has low aquifer potential with abrupt lithological changes, possibly dominated by shale due to high S and low ρ$_L$ [85]. On the other hand, the NE–SW side shows a higher probability of sandy lithology with low S and high ρ$_L$. The total transverse resistance (TR) decreases toward the NE side, while the maximum value is observed along the SW side. TR ranges from ≥10 Ωm^2 to ≤2,800,000 Ωm^2, with VES-18, 19, 20, and 21 having the highest values (1,400,000 Ωm^2 to 2,800,000 Ωm^2), and a minimum recording of 10 Ωm^2 to 60,000 Ωm^2 (Figure 14c). The transverse resistivity (ρ$_T$) follows a similar trend to TR, with a decrease in resistivity toward the NE side, as observed in VES-14, 15, 16, 17, 22, and 23. The ρ$_T$ ranges from ≥10 Ωm to ≤6000 Ωm, with the highest value being 4000–6000 Ωm and the lowest 10 Ωm to 800 Ωm (Figure 14d). TR and ρ$_T$ clearly differentiate the lithological units on the NE and SW sides, with the NE side showing low permeable lithology of clayey sand, while the SW side exhibits sandstone, indicating good aquifer potential and good water quality [55,85,87].

The macroanisotropy, representing lithological distinctions based on hydraulic parameters, ranges from ≥01 to ≤12 (Figure 15a). The NE side has a low-value range of ≥01 to ≤05, while the SW side records the maximum value of ≥09 to ≤12. The macroanisotropy aligns with the pseudosection, geo-log, and SDR, clearly distinguishing different hydrological units on the NE and SW sides. The overall true resistivity section depicts a clear demarcation of low and high resistivity values, ranging from ≥20 Ωm to ≤450 Ωm (Figure 15b). The SW side shows low resistivity (10 Ωm to 100 Ωm), while the NE side exhibits high resistivity (300 Ωm to 450 Ωm). The NE side is likely dominated by sandy clay to sandstone, while the SE side contains a higher proportion of clayey sand and sandy clay [33,88].
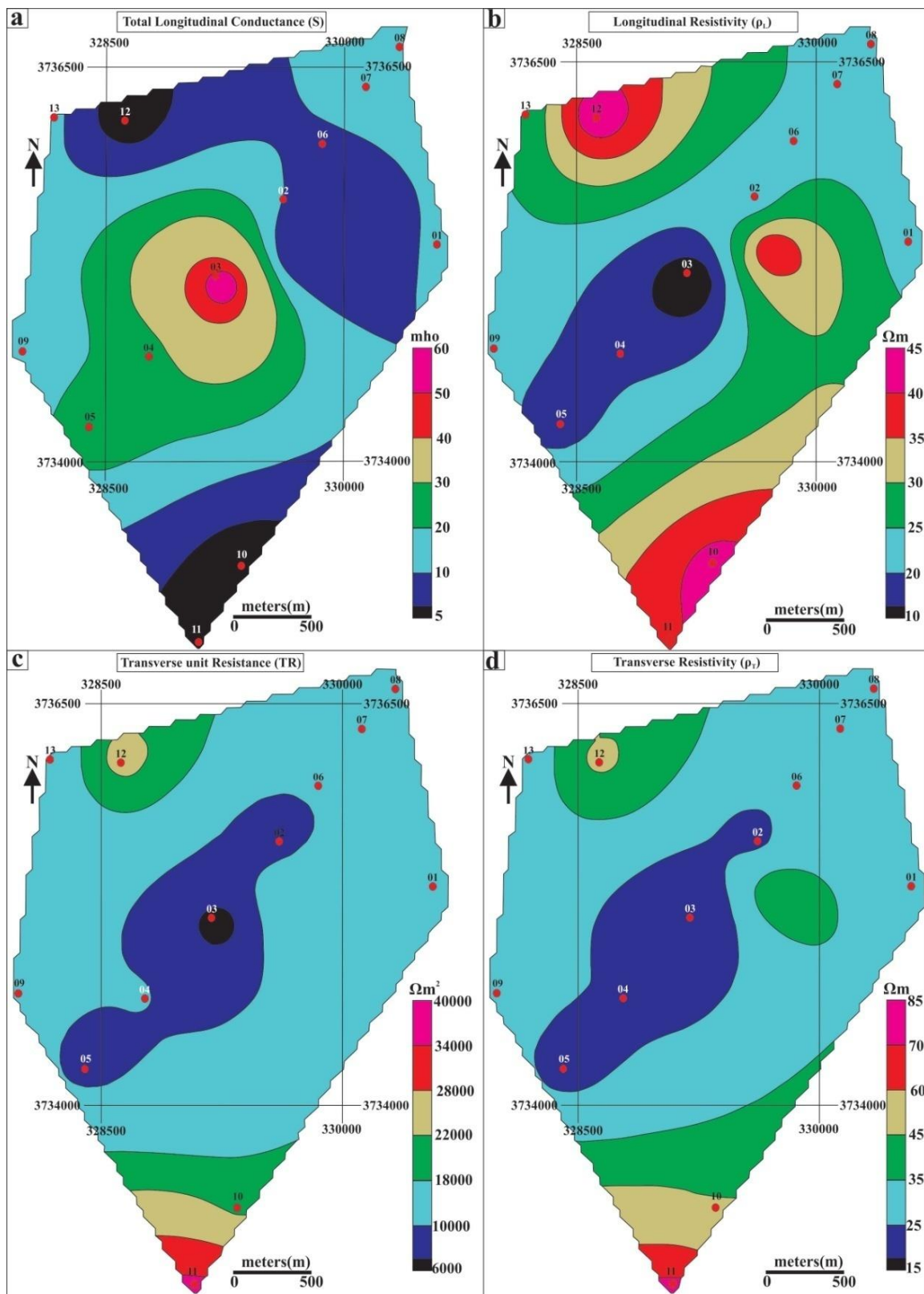
Figure 12. Hydraulic parameters of Bara Kahu Area 1, (**a**) Total longitudinal conductance with increasing trend along SW side toward the center, (**b**) Longitudinal resistivity showing decreasing trend along SW side toward center, (**c**) Total transverse resistance with decreasing trend along SW side, (**d**) Transverse resistivity with decrease trend along SW side and increase in value recorded from SE to NW.
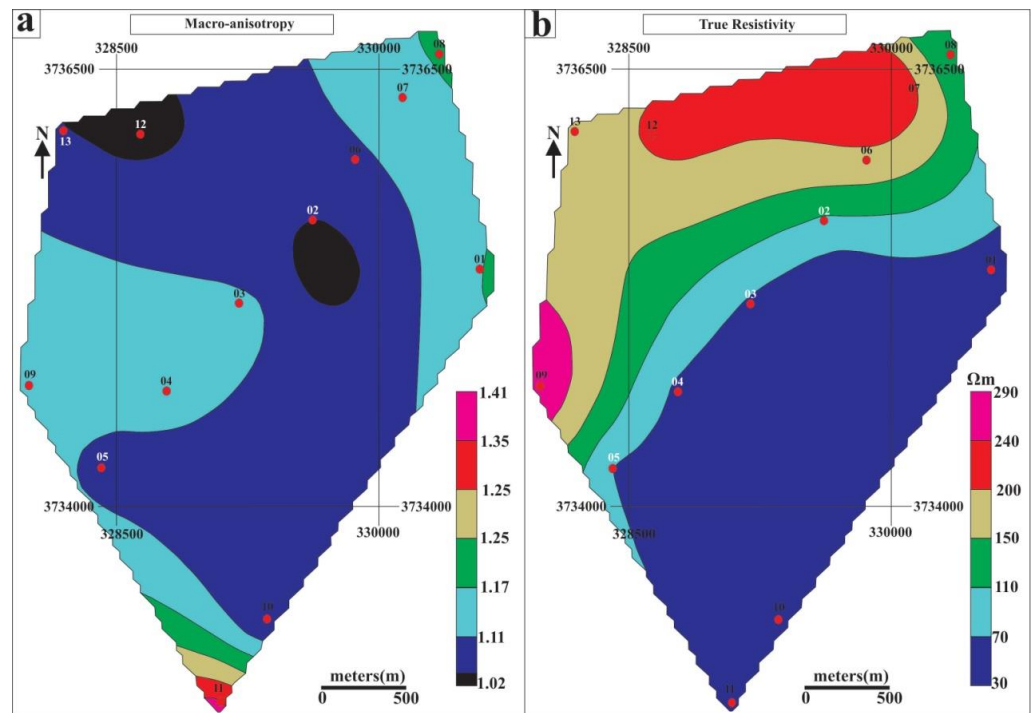
Figure 13. (**a**) Macroanisotropy of Area 1 displaying differentiating lithologies along SE and NW side, (**b**) True resistivity of Area 1 demarcating mean resistivity distribution along the area.
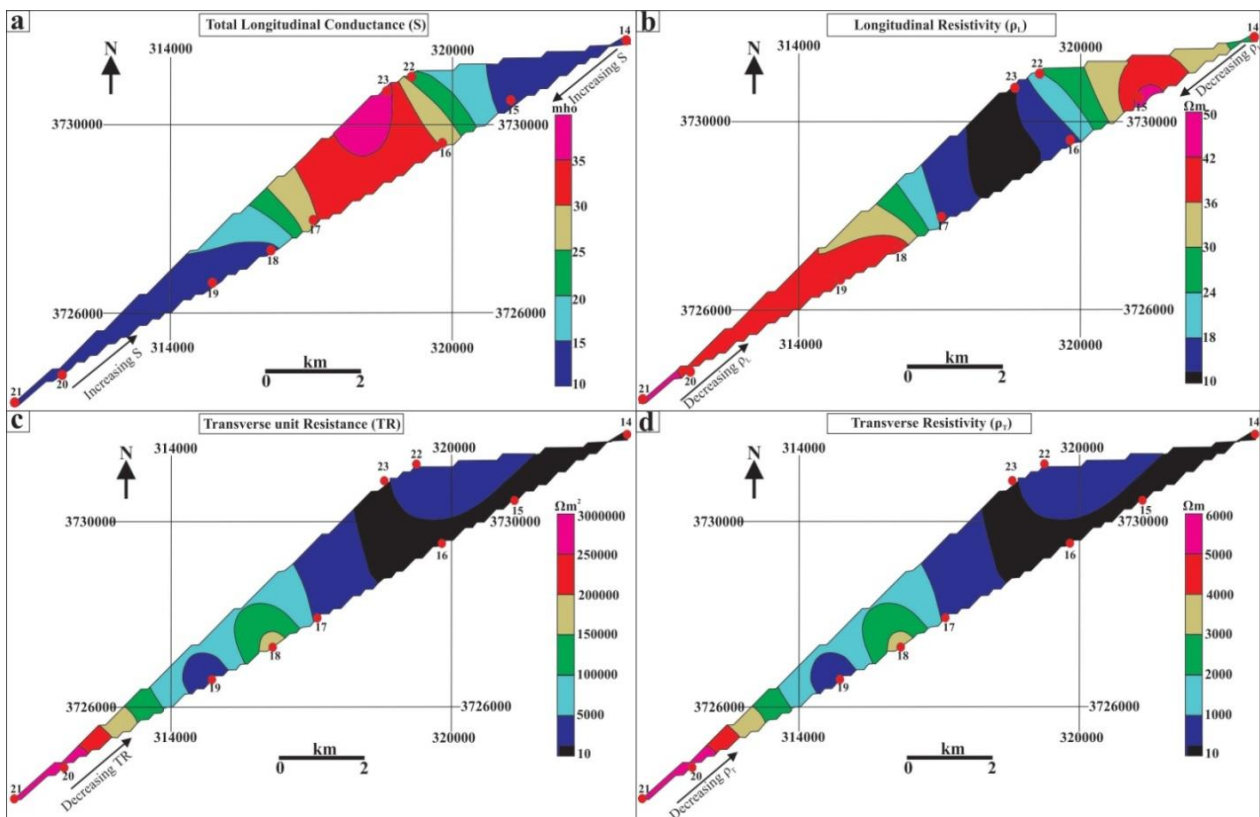
Figure 14. Hydraulic parameters of Area 2, (**a**) total longitudinal conductance deciphering minimum values in SW and NE side with maximum at center, (**b**) longitudinal resistivity recorded low at center and high along SW and NE side, (**c**) transverse resistance of low value along NE side with maximum toward SW, (**d**) transverse resistivity of minimum value along NE side with maximum at SW.
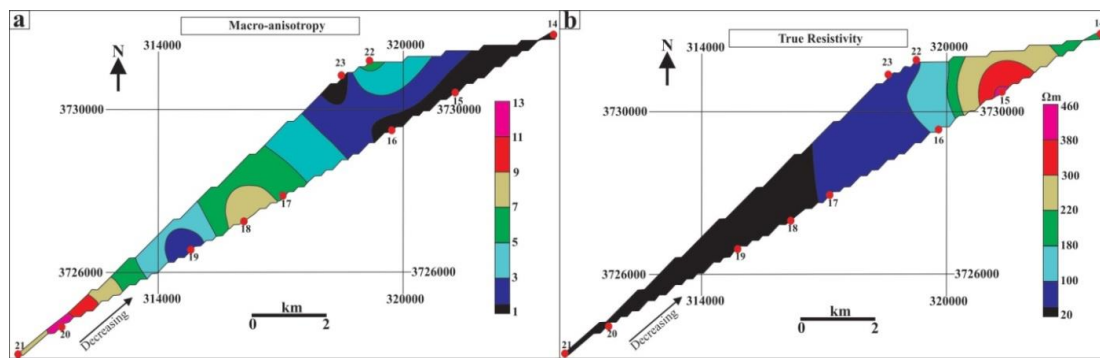
Figure 15. (**a**) Macroanisotropy along Area 2 with low value at NE side deciphering different lithological units, (**b**) True resistivity of Area 2 having minimum value at SW side and maximum value at NE side confirming same trend as macroanisotropy.

4.6. Aquifer Thickness vs. Depth

The aquifer thickness and depth map provides valuable insights into the distribution of potable aquifers, which could be tapped in the near future for long-term water supply. The data for aquifer thickness and depth were obtained from inverted resistivity curves using IPI2win.

In Area 1, the aquifer thickness varies from $\geq$10 m to $\leq$220 m, with the maximum thickness observed on the SE and NE sides, ranging from 160 to 220 m (Figure 16a). Conversely, the thickness decreases toward the SW side, ranging from 10 to 40 m. The aquifer depth ranges from 10 to 220 m, with the minimum depth located on the SE to SW side (10 to 20 m), while the NE side exhibits greater depths of up to 200 m (Figure 16b). Based on the thickness and depth map, the SE side of Area 1 appears to be a promising location for a potential reservoir.
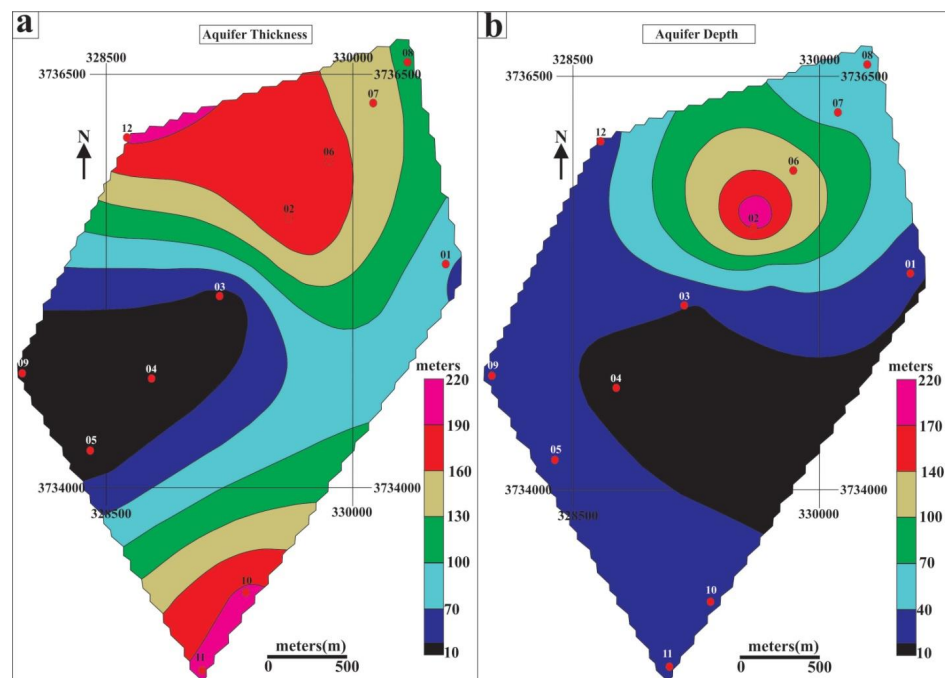

Figure 16. Aquifer thickness and depth map of Area 1, (**a**) Aquifer thickness demarcating maximum value along SE and NW side, (**b**) Aquifer maximum along NE–NW side with low depth assured at SE–SW side.

In Area 2, the thickness of the aquifer decreases from the SW to NE side, ranging from $\geq$30 m to $\leq$300 m toward the center, with maximum thickness along VES-15 and 18

(250–300 m) (Figure 17a). The depth of the aquifer increases from the SW and NE toward the center, varying from $\geq$10 m to $\leq$300 m, with the maximum depth along VES-17 and 18 (200–300 m), and the minimum depth of 10–20 m along VES-14, 15, 20, and 21 (Figure 17b). The thickness and depth maps indicate that the NE and SW sides are potential areas for groundwater estimation.
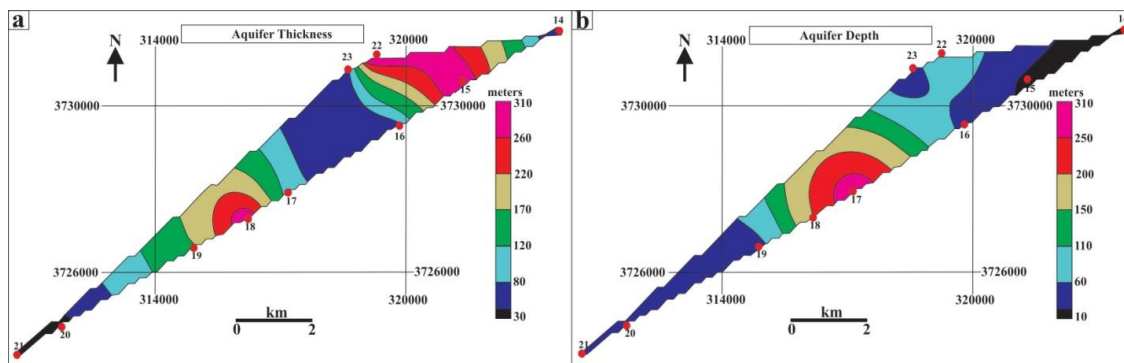

Figure 17. Aquifer thickness and depth map of Area 2, (**a**) Aquifer thickness deciphering increase in value at SW and NE side with minimum value at center, (**b**) Aquifer depth showing maximum depth at center with minimum at SW and NE.

Linear regression (R^2) values were calculated to examine the relationship between dependent and independent variables [89]. The dependent variable, resistivity, is influenced by factors such as lithology, thickness, depth, porosity, and water chemistry [20–23,89]. The R^2 values for Area 1 are 0.098 for thickness and 0.1 for depth (Figure 18a,b), while for Area 2, the values are 0.119 for thickness and 0.283 for depth (Figure 18c,d). These R^2 values suggest that thickness and depth have a relatively minor influence on resistivity, accounting for approximately 10–20% of the variation. On the other hand, 80–90% of the resistivity variation is attributed to factors such as permeability, porosity, and groundwater chemistry. Hence, the R^2 value indicates that any alterations in resistivity are primarily due to the underground aquifer characteristics and potential.
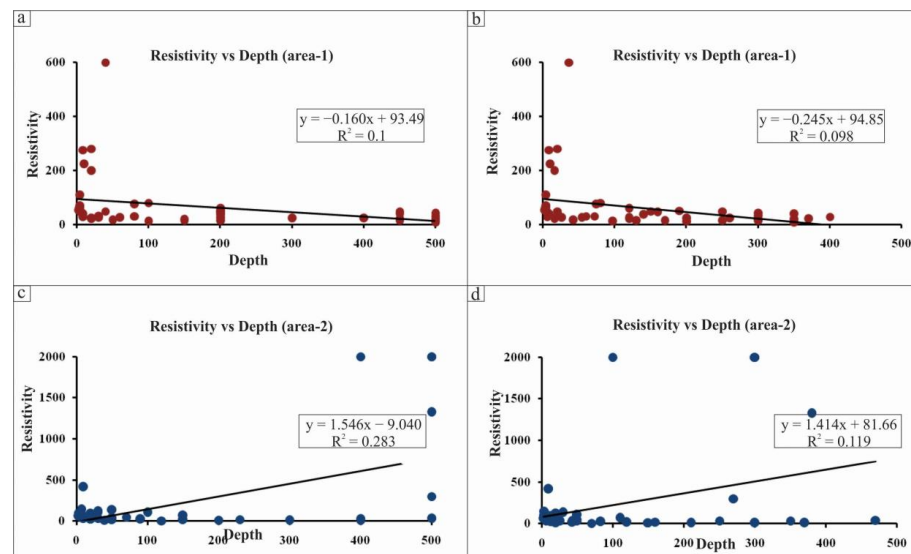

Figure 18. Linear regression (R^2) value of the study area, (**a**) R^2 of Area 1 showing value of 0.1 inferring 10% dependence of resistivity vs. depth, (**b**) R^2 of Area 1 having value of 0.98 infers 9.8% dependency of resistivity vs. thickness, (**c**) R^2 of Area 2 shows value of 0.283 referring to 28.3% approach of resistivity vs. depth, (**d**) R^2 of Area 2 shows value of 0.119 inferring 11.9% dependency of resistivity vs. thickness.

5. Conclusions

In conclusion, the geophysical resistivity survey conducted in the Islamabad area (targeting Area 1: Bara Kahu and Area 2: Aabpara to G13) up to a maximum depth of 500 m has provided valuable insights into the aquifer potential. The data indicate that the area harbors good potential for drinkable water of high quality, with aquifers comprising a mixture of sandy and clayey lithological compositions, giving rise to both shallow and deep confined and unconfined aquifers.

- The resistivity logs reveal the presence of various lithological units, including sandstone, shale, clay, sandy clay, clayey sand, and shaley clay. The main potential aquifer horizons are identified as sandstone, sandy clay, and clayey sand, while shaley clay appears to be a shallow aquifer of poor quality.
- The detailed geologs of Area 1 (Bara Kahu) and Area 2 (Aabpara to G13) indicate the presence of both shallow and deeper aquifers, with sandstone and sandy clay dominating at different depths. The P-I logs show shallow aquifers at 10–20 m depth and deeper aquifers at depths greater than 50 m. P-II logs reveal the presence of unconfined aquifers with clayey sand as the shallow aquifer and deeper aquifers consisting of sandy clay. P-III logs indicate the dominance of semi-confined aquifers with shallow potential in sandstone and sandy clay and deeper horizons in clayey sand.
- The pseudosections of both areas highlight good potential for groundwater, with various aquifer types and depths ranging from 10 to 40 m. The NE side of the study areas consistently shows better aquifer potential compared to the SW side, owing to the presence of maximum sandstone.
- The resistivity data and true resistivity sections further support the presence of distinct lithological units, with sandy beds dominating along the NE and NW sides, while clay/shale is prevalent in the SE–SW region.
- The longitudinal conductance (S) and longitudinal resistivity (ρL) analyses confirm the presence of sandy units with good aquifer potential along the NW and SE sides. Transverse resistance (TR) and transverse resistivity (ρT) indicate the presence of permeable units along the NW and SE sides, while impermeable units dominate the SW side. The macroanisotropy and true resistivity maps provide additional evidence of lithological variations, with NE and SW sides showing different hydrological units.
- The aquifer thickness and depth maps show variations in aquifer thickness ranging from 10 to 200 m, with maximum thickness recorded along the SE and NW sides, while the NE side exhibits greater depth. These maps highlight the SE side as a promising area for potential reservoirs.
- The linear regression analysis suggests that depth and thickness have a relatively minor influence, accounting for only 10% to 20% of the resistivity variation. The major controlling factors on resistivity are groundwater characteristics, permeability, porosity, and lithological units, which account for 80% to 90% of the observed resistivity changes.

In summary, the geophysical resistivity survey has successfully delineated the aquifer potential in the study area, providing valuable information for future water supply planning and resource management.

6. Recommendations

To comprehensively study Islamabad's rough and undulating topography and vulnerable subsurface lithology, a detailed ground magnetic and gravity survey should be conducted to understand subsurface tectonics and lithological distributions. Additionally, a detailed resistivity survey covering the entire area with a regular grid interval of 1 km × 1 km should be performed to delineate aquifers up to a depth of 1 km.

Advanced remote sensing techniques should be used to create a drainage map, allowing for a better understanding of surface water distribution. To obtain overall geological coverage and enable subsequent 3D comparisons with subsurface data, Islamabad should

be mapped at a scale of 1:50,000. To confirm the potential and characteristics of promising aquifer locations indicated by geophysical surveys, test drilling should be carried out. Water geochemical and biological tests should also be conducted, and hazard risk maps for different elements and biological factors should be produced. To efficiently assess aquifer risk, geophysical signatures for different factors can be developed, providing a cost-effective means of identifying potential contaminant flow and risk factors in the surrounding area.

References

1. Yan, D.; Yao, M.; Ludwig, F.; Kabat, P.; Huang, H.Q.; Hutjes, R.W.; Werners, S.E. Exploring future water shortage for large river basins under different water allocation strategies. *Water Resour. Manag.* **2018**, *32*, 3071–3086. [CrossRef]
2. Oki, T.; Kanae, S. Global hydrological cycles and world water resources. *Science* **2006**, *313*, 1068–1072. [CrossRef] [PubMed]
3. Plummer, C.C.; Carlson, D.; Hammersley, L. *Physical Geology*; McGraw-Hill/Education: New York, NY, USA, 2016.
4. Casper, J.K. *Water and Atmosphere: The Lifeblood of Natural Systems*; Infobase Publishing: New York, NY, USA, 2007.
5. Orimoloye, I.R.; Belle, J.A.; Olusola, A.O.; Busayo, E.T.; Ololade, O.O. Spatial assessment of drought disasters, vulnerability, severity and water shortages: A potential drought disaster mitigation strategy. *Nat. Hazards* **2021**, *105*, 2735–2754. [CrossRef]
6. Salehi, M. Global water shortage and potable water safety; Today's concern and tomorrow's crisis. *Environ. Int.* **2022**, *158*, 106936. [CrossRef]
7. López-Pacheco, I.Y.; Silva-Núñez, A.; Salinas-Salazar, C.; Arévalo-Gallegos, A.; Lizarazo-Holguin, L.A.; Barceló, D.; Iqbal, H.M.; Parra-Saldívar, R. Anthropogenic contaminants of high concern: Existence in water resources and their adverse effects. *Sci. Total Environ.* **2019**, *690*, 1068–1088. [CrossRef]
8. Li, P.; Karunanidhi, D.; Subramani, T.; Srinivasamoorthy, K. Sources and consequences of groundwater contamination. *Arch. Environ. Contam. Toxicol.* **2021**, *80*, 1–10. [CrossRef]
9. Carrard, N.; Foster, T.; Willetts, J. Groundwater as a source of drinking water in southeast Asia and the Pacific: A multi-country review of current reliance and resource concerns. *Water* **2019**, *11*, 1605. [CrossRef]
10. Zhang, Z.; Wang, W. Managing aquifer recharge with multi-source water to realize sustainable management of groundwater resources in Jinan, China. *Environ. Sci. Pollut. Res.* **2021**, *28*, 10872–10888. [CrossRef]
11. Zhang, Z.; Li, Y.; Wang, X.; Liu, Y.; Tang, W.; Ding, W.; Han, Q.; Shang, G.; Wang, Z.; Chen, K. Investigating River health across mountain to urban transitions using Pythagorean fuzzy cloud technique under uncertain environment. *J. Hydrol.* **2023**, *620*, 129426. [CrossRef]
12. Sarah, S.; Ahmed, S.; Violette, S.; de Marsily, G. Groundwater sustainability challenges revealed by quantification of contaminated groundwater volume and aquifer depletion in hard rock aquifer systems. *J. Hydrol.* **2021**, *597*, 126286. [CrossRef]
13. Brindha, K.; Schneider, M. Impact of urbanization on groundwater quality. In *GIS and Geostatistical Techniques for Groundwater Science*; Elsevier: Amsterdam, The Netherlands, 2019; pp. 179–196.
14. Karunanidhi, D.; Subramani, T.; Srinivasamoorthy, K.; Yang, Q. Environmental chemistry, toxicity and health risk assessment of groundwater: Environmental persistence and management strategies. *Environ. Res.* **2022**, *214*, 113884. [CrossRef]
15. Akhtar, N.; Syakir Ishak, M.I.; Bhawani, S.A.; Umar, K. Various natural and anthropogenic factors responsible for water quality degradation: A review. *Water* **2021**, *13*, 2660. [CrossRef]

16. Rao, P.S.C.; Jawitz, J.W.; Enfield, C.G.; Falta, R., Jr.; Annable, M.D.; Wood, A.L. Technology integration for contaminated site remediation: Clean-up goals and performance criteria. *Groundw. Qual. Nat. Enhanc. Restor. Groundw. Pollut.* **2001**, *275*, 571–578.

17. Khorrami, M.; Malekmohammadi, B. Effects of excessive water extraction on groundwater ecosystem services: Vulnerability assessments using biophysical approaches. *Sci. Total Environ.* **2021**, *799*, 149304. [CrossRef]

18. Díaz-Alcaide, S.; Martínez-Santos, P. Advances in groundwater potential mapping. *Hydrogeol. J.* **2019**, *27*, 2307–2324. [CrossRef]

19. Zaher, M.A.; Younis, A.; Shaaban, H.; Mohamaden, M.I. Integration of geophysical methods for groundwater exploration: A case study of El Sheikh Marzouq area, Farafra Oasis, Egypt. *Egypt. J. Aquat. Res.* **2021**, *47*, 239–244. [CrossRef]

20. Lubang, J.; Liu, H.; Chen, R. Combined Application of Hydrogeological and Geoelectrical Study in Groundwater Exploration in Karst-Granite Areas, Jiangxi Province. *Water* **2023**, *15*, 865. [CrossRef]

21. Mohamed, A.; Othman, A.; Galal, W.F.; Abdelrady, A. Integrated geophysical approach of groundwater potential in Wadi Ranyah, Saudi Arabia, using gravity, electrical resistivity, and remote-sensing techniques. *Remote Sens.* **2023**, *15*, 1808. [CrossRef]

22. Nagaiah, E.; Sonkamble, S.; Chandra, S. Electrical geophysical techniques pin-pointing the bedrock fractures for groundwater exploration in granitic hard rocks of Southern India. *J. Appl. Geophys.* **2022**, *199*, 104610. [CrossRef]

23. Aliou, A.-S.; Dzikunoo, E.A.; Yidana, S.M.; Loh, Y.; Chegbeleh, L.P. Investigation of Geophysical Signatures for Successful Exploration of Groundwater in Highly Indurated Sedimentary Basins: A Look at the Nasia Basin, NE Ghana. *Nat. Resour. Res.* **2022**, *31*, 3223–3251. [CrossRef]

24. Bhatnagar, S.; Taloor, A.K.; Roy, S.; Bhattacharya, P. Delineation of aquifers favorable for groundwater development using Schlumberger configuration resistivity survey techniques in Rajouri district of Jammu and Kashmir, India. *Groundw. Sustain. Dev.* **2022**, *17*, 100764. [CrossRef]

25. Brahmi, S.; Baali, F.; Hadji, R.; Brahmi, S.; Hamad, A.; Rahal, O.; Zerrouki, H.; Saadali, B.; Hamed, Y. Assessment of groundwater and soil pollution by leachate using electrical resistivity and induced polarization imaging survey, case of Tebessa municipal landfill, NE Algeria. *Arab. J. Geosci.* **2021**, *14*, 249. [CrossRef]

26. Islami, N.; Irianti, M.; Fakhruddin, F.; Azhar, A.; Nor, M. Application of geoelectrical resistivity method for the assessment of shallow aquifer quality in landfill areas. *Environ. Monit. Assess.* **2020**, *192*, 249. [CrossRef] [PubMed]

27. Chibuike, A.; Chukwu, A.C.; Kelechi, O.K. Efficiency and limitation of vertical electrical sounding in evaluation of groundwater potential in fractured shale terrain: A case study of Abakaliki Area Lower Benue Trough Nigeria. *Environ. Monit. Assess.* **2023**, *195*, 158. [CrossRef]

28. Joel, E.S.; Olasehinde, P.I.; Adagunodo, T.A.; Omeje, M.; Oha, I.; Akinyemi, M.L.; Olawole, O.C. Geo-investigation on groundwater control in some parts of Ogun state using data from Shuttle Radar Topography Mission and vertical electrical soundings. *Heliyon* **2020**, *6*, e03327. [CrossRef] [PubMed]

29. Soomro, A.; Qureshi, A.L.; Jamali, M.A.; Ashraf, A. Groundwater investigation through vertical electrical sounding at hilly area from Nooriabad toward Karachi. *Acta Geophys.* **2019**, *67*, 247–261. [CrossRef]

30. Omeje, E.T.; Ugbor, D.O.; Ibuot, J.C.; Obiora, D.N. Assessment of groundwater repositories in Edem, Southeastern Nigeria, using vertical electrical sounding. *Arab. J. Geosci.* **2021**, *14*, 421. [CrossRef]

31. de Almeida, A.; Maciel, D.F.; Sousa, K.F.; Nascimento, C.T.C.; Koide, S. Vertical electrical sounding (VES) for estimation of hydraulic parameters in the porous aquifer. *Water* **2021**, *13*, 170. [CrossRef]

32. Rashid, M.; Ahmad, W.; Zeb, M.J.; Haider, N.; Khan, A.; Khan, S. Determination of Underground Structure and Migration of Hot Plumes Contaminating Fresh Water Using Vertical Electrical Survey (VES) and Magnetic Survey, A Case Study of Tattapani Thermal Spring, Azad Kashmir. *Int. J. Econ. Environ. Geol.* **2019**, *10*, 84–92.

33. Akinrinade, O.J.; Adesina, R.B. Hydrogeophysical investigation of groundwater potential and aquifer vulnerability prediction in basement complex terrain–A case study from Akure, Southwestern Nigeria. *Mater. Geoenviron.* **2016**, *63*, 55–66. [CrossRef]

34. Sanuade, O.A.; Arowoogun, K.I.; Amosun, J.O. A review on the use of geoelectrical methods for characterization and monitoring of contaminant plumes. *Acta Geophys.* **2022**, *70*, 2099–2117. [CrossRef]

35. Kumar, D.; Mondal, S.; Warsi, T. Deep insight to the complex aquifer and its characteristics from high resolution electrical resistivity tomography and borehole studies for groundwater exploration and development. *J. Earth Syst. Sci.* **2020**, *129*, 68. [CrossRef]

36. Lee, S.C.H.; Noh, K.A.M.; Zakariah, M.N.A. High-resolution electrical resistivity tomography and seismic refraction for ground-water exploration in fracture hard rocks: A case study in Kanthan, Perak, Malaysia. *J. Asian Earth Sci.* **2021**, *218*, 104880. [CrossRef]

37. Hussain, Z.; Wang, Z.; Wang, J.; Yang, H.; Arfan, M.; Hassan, D.; Wang, W.; Azam, M.I.; Faisal, M. A comparative appraisal of classical and holistic water scarcity indicators. *Water Resour. Manag.* **2022**, *36*, 931–950. [CrossRef]

38. Qureshi, A.S. Groundwater Governance in Pakistan: From Colossal Development to Neglected Management. *Water* **2020**, *12*, 3017. [CrossRef]

39. Ahmed, K.; Shamsuddin, S.; Demirel, M.C.; Nadeem, N.; Najeebullah, K. The changing characteristics of groundwater sustainability in Pakistan from 2002 to 2016. *Hydrogeol. J.* **2019**, *27*, 2485–2496. [CrossRef]

40. Ebrahim, Z.T. *Is Pakistan Running Dry? Water Issues in Himalayan South Asia: Internal Challenges, Disputes and Transboundary Tensions*; Springer: Berlin/Heidelberg, Germany, 2020; pp. 153–181.

41. Iqbal, A.R. Water Shortage in Pakistan-A Crisis around the Corner. *Inst. Strateg. Stud. Res. Anal. (ISSRA)* **2010**, *2*, 1–13.

42. Briscoe, J.; Qamar, U.; Contijoch, M.; Amir, P.; Blackmore, D. *Pakistan's Water Economy: Running Dry*; Oxford University Press: Karachi, Pakistan, 2006.

43. Saleem, S.; Ali, W.; Afzal, M.S. Status of Drinking Water Quality and its Contamination in Pakistan. *J. Environ. Res.* **2018**, *2*, 6.

44. Daud, M.; Nafees, M.; Ali, S.; Rizwan, M.; Bajwa, R.A.; Shakoor, M.B.; Arshad, M.U.; Chatha, S.A.S.; Deeba, F.; Murad, W. Drinking water quality status and contamination in Pakistan. *BioMed Res. Int.* **2017**, *2017*, 7908183. [CrossRef]

45. Nabeela, F.; Azizullah, A.; Bibi, R.; Uzma, S.; Murad, W.; Shakir, S.K.; Ullah, W.; Qasim, M.; Häder, D.-P. Microbial contamination of drinking water in Pakistan—A review. *Environ. Sci. Pollut. Res.* **2014**, *21*, 13929–13942. [CrossRef]

46. Force, Water Sector Task. *A Productive and Water-Secure Pakistan: Infrastructure, Institutions, Strategy, the Report of the Water Sector Task Force of the Friends of Democratic Pakistan*; Force, Water Sector Task: Islamabad, Pakistan, 2012.

47. Iqbal, N.; Din, S.; Ashraf, M.; Asmat, S. Hydrological Assessment of Surface and Groundwater Resources of Islamabad, Pakistan. *Pak. Counc. Res. Water Resour. (PCRWR) Islamabad* **2023**, 76.

48. Sohail, M.T.; Mahfooz, Y.; Azam, K.; Yen, Y.; Genfu, L.; Fahad, S. Impacts of urbanization and land cover dynamics on underground water in Islamabad, Pakistan. *Desalin Water Treat* **2019**, *159*, 402–411. [CrossRef]

49. Khan, J.; Ren, X.; Hussain, M.A.; Jan, M.Q. Monitoring Land Subsidence Using PS-InSAR Technique in Rawalpindi and Islamabad, Pakistan. *Remote Sens.* **2022**, *14*, 3722. [CrossRef]

50. Hassan, D.; Rais, M.N.; Ahmed, W.; Bano, R.; Burian, S.J.; Ijaz, M.W.; Bhatti, F.A. Future water demand modeling using water evaluation and planning: A case study of the Indus Basin in Pakistan. *Sustain. Water Resour. Manag.* **2019**, *5*, 1903–1915. [CrossRef]

51. Khan, U.; Janjuhah, H.T.; Kontakiotis, G.; Rehman, A.; Zarkogiannis, S.D. Natural Processes and Anthropogenic Activity in the Indus River Sedimentary Environment in Pakistan: A Critical Review. *J. Mar. Sci. Eng.* **2021**, *9*, 1109. [CrossRef]

52. Water Resource Division, M.O.W.R. National Water Policy. *Policy Div.* **2018**, 1–44.

53. Shah, S.H.I.A.; Jianguo, Y.; Jahangir, Z.; Tariq, A.; Aslam, B. Integrated geophysical technique for groundwater salinity delineation, an approach to agriculture sustainability for Nankana Sahib Area, Pakistan. *Geomat. Nat. Hazards Risk* **2022**, *13*, 1043–1064. [CrossRef]

54. Fajana, A. Integrated geophysical investigation of aquifer and its groundwater potential in phases 1 and 2, Federal University Oye-Ekiti, south-western basement complex of Nigeria. *Model. Earth Syst. Environ.* **2020**, *6*, 1707–1725. [CrossRef]

55. Echogdali, F.Z.; Boutaleb, S.; Bendarma, A.; Saidi, M.E.; Aadraoui, M.; Abioui, M.; Ouchchen, M.; Abdelrahman, K.; Fnais, M.S.; Sajinkumar, K.S. Application of analytical hierarchy process and geophysical method for groundwater potential mapping in the Tata basin, Morocco. *Water* **2022**, *14*, 2393. [CrossRef]

56. Ahmed, Z.; Ansari, M.T.; Zahir, M.; Shakir, U.; Subhan, M. Hydrogeophysical investigation for groundwater potential through Electrical Resistivity Survey in Islamabad, Pakistan. *J. Geogr. Soc. Sci. JGSS* **2020**, *2*, 147–163.

57. Qadir, A.; Amjad, M.R.; Khan, T.; Zafar, M.; Hasham, M.; Khan, U.A.; Khattak, S.A.; Ahmad, I. Demarcation of groundwater potential zones by electrical resistivity survey (ERS) islamabad, Pakistan. *Int. J. Econ. Environ. Geol.* **2018**, *9*, 39–44.

58. Lisa, M.; Khan, S.A.; Khwaja, A.A. Focal mechanism study of north Potwar deformed zone, Pakistan. *Acta Seismol. Sin.* **2004**, *17*, 255–261. [CrossRef]

59. Khan, S.; Waseem, M.; Khan, M.A. A Seismic Hazard Map Based on Geology and Shear-wave Velocity in Rawalpindi–Islamabad, Pakistan. *Acta Geol. Sin. Engl. Ed.* **2021**, *95*, 659–673. [CrossRef]

60. Adeel, M.B.; Nizamani, Z.A.; Aaqib, M.; Khan, S.; Rehman, J.U.; Bhusal, B.; Park, D. Estimation of V S30 using shallow depth time-averaged shear wave velocity of Rawalpindi–Islamabad, Pakistan. *Geomat. Nat. Hazards Risk* **2023**, *14*, 1–21. [CrossRef]

61. Shah, S.M.I. *Stratigraphy of Pakistan*, 22nd ed.; Geological Survey of Pakistan Publication Directorate: Quetta, Pakistan, 2009; Volume 22, p. 381.

62. Sheikh, I.M.; Pasha, M.K.; Williams, V.S.; Raza, S.Q.; Khan, K.S. Environmental geology of the Islamabad-Rawalpindi area, northern Pakistan. In *Regional Studies of the Potwar-Plateau Area, Northern Pakistan. Bull. G*; U.S. Department of the Interior: Washington, DC, USA, 2008; Volume 2078.

63. MonaLisa; Khwaja, A.A. Tectonic Model of NW Himalayan Fold and Thrust Belt on the basis of Focal Mechanism studies. *Pak. J. Meteorol.* **2005**, *2*, 9–50.

64. Williams, V.S.; Pasha, M.K.; Sheikh, I.M. *Geologic Map of the Islamabad-Rawalpindi Area, Punjab, Northern Pakistan*; The Survey; USGS: Reston, VA, USA, 1999. Available online: https://pubs.usgs.gov/publication/ofr9947 (accessed on 19 November 2023).

65. Shah, S.H.; Khan, N.A.; Bhatti, M.A. Geological Map of Islamabad and surrounding. In *Geological Survey of Pakistan Special Map Series No. 1*; Geological Survey of Pakistan: Quetta, Pakistan, 2000.

66. Rashid, M.; Ahmed, W.; Anwar, S.; Abbas, S.A.; Waseem, M.; Khan, S. Groundwater resource characterization using geo-electrical survey: A case study of Rawlakot, Azad Jammu and Kashmir. *J. Himal. Earth Sci.* **2017**, *50*, 125–136.

67. Gómez, D.G.; Ochoa, C.G.; Godwin, D.; Tomasek, A.A.; Zamora Re, M.I. Soil Water Balance and Shallow Aquifer Recharge in an Irrigated Pasture Field with Clay Soils in the Willamette Valley, Oregon, USA. *Hydrology* **2022**, *9*, 60. [CrossRef]

68. Islam, I.; Ahmed, W.; Rashid, M.U.; Orakzai, A.U.; Ditta, A. Geophysical and geotechnical characterization of shallow subsurface soil: A case study of University of Peshawar and surrounding areas. *Arab. J. Geosci.* **2020**, *13*, 949. [CrossRef]

69. Oyeyemi, K.D.; Aizebeokhai, A.P.; Metwaly, M.; Omobulejo, O.; Sanuade, O.A.; Okon, E.E. Assessing the suitable electrical resistivity arrays for characterization of basement aquifers using numerical modeling. *Heliyon* **2022**, *8*, e09427. [CrossRef]

70. Singh, U.; Sharma, P.K. Study on geometric factor and sensitivity of subsurface for different electrical resistivity Tomography Arrays. *Arab. J. Geosci.* **2022**, *15*, 560. [CrossRef]

71. Mirzaei, L.; Hafizi, M.K.; Riahi, M.A. Application of Dipole–Dipole, Schlumberger, and Wenner–Schlumberger Arrays in Groundwater Exploration in Karst Areas Using Electrical Resistivity and IP Methods in a Semi-arid Area, Southwest Iran. In *Water Resources in Arid Lands: Management and Sustainability*; Springer: Berlin/Heidelberg, Germany, 2021; pp. 81–89.

72. Bobachev, C. *IPI2Win: A Windows Software for an Automatic Interpretation of Resistivity Sounding Data*; Moscow State University: Moscow, Russia, 2002.

73. Rashid, M.; Ahmed, W.; Zeb, M.J.; Mahmood, Z.; Khan, S.; Waseem, M. Geoelectrical and magnetic survey of Tatta Pani thermal spring: A case study from Kotli District, Jammu and Kashmir, Pakistan. *Geomech. Geophys. Geo-Energy Geo-Resour.* **2021**, *7*, 41. [CrossRef]

74. Hasan, M.; Shang, Y.; Jin, W.; Akhter, G. Estimation of hydraulic parameters in a hard rock aquifer using integrated surface geoelectrical method and pumping test data in southeast Guangdong, China. *Geosci. J.* **2021**, *25*, 223–242. [CrossRef]

75. Telford, W.M.; Geldart, L.P.; Sheriff, R.E. *Applied Geophysics*, 2nd ed.; Cambridge University Press: Cambridge, UK, 1990; Volume 1, p. 770.

76. Metwaly, M.; Elawadi, E.; Moustafal, S.S.; Al Fouzan, F.; Mogren, S.; Al Arifi, N. Groundwater exploration using geoelectrical resistivity technique at Al-Quwy'yia area central Saudi Arabia. *Int. J. Phys. Sci.* **2012**, *7*, 317–326. [CrossRef]

77. George, N.J. Modelling the trends of resistivity gradient in hydrogeological units: A case study of alluvial environment. *Model. Earth Syst. Environ.* **2021**, *7*, 95–104. [CrossRef]

78. Ghani, M.; Atif, M.; Saeed, M.; Rasheed, M.; Abbas, S.A.; Jan, I.U.; Aziz, M. Geo-electrical sounding for subsurface lithological investigation and modeling for groundwater exploration in Sheikhmanda Kili region, Northern Quetta, Pakistan. *Himal Geol* **2022**, *43*, 40–50.

79. Mainoo, P.A.; Manu, E.; Yidana, S.M.; Agyekum, W.A.; Stigter, T.; Duah, A.A.; Preko, K. Application of 2D-Electrical resistivity tomography in delineating groundwater potential zones: Case study from the voltaian super group of Ghana. *J. Afr. Earth Sci.* **2019**, *160*, 103618. [CrossRef]

80. Magara, K. Comparison of porosity-depth relationships of shale and sandstone. *J. Pet. Geol.* **1980**, *3*, 175–185. [CrossRef]

81. Scherer, M. Parameters influencing porosity in sandstones: A model for sandstone porosity prediction. *AAPG Bull.* **1987**, *71*, 485–491. [CrossRef]

82. Mohammed, M.; Senosy, M.; Abudeif, A. Derivation of empirical relationships between geotechnical parameters and resistivity using electrical resistivity tomography (ERT) and borehole data at Sohag University site, upper Egypt. *J. Afr. Earth Sci.* **2019**, *158*, 103563. [CrossRef]

83. Uhlemann, S.; Kuras, O.; Richards, L.A.; Naden, E.; Polya, D.A. Electrical resistivity tomography determines the spatial distribution of clay layer thickness and aquifer vulnerability, Kandal Province, Cambodia. *J. Asian Earth Sci.* **2017**, *147*, 402–414. [CrossRef]

84. Nguyen, F.; Garambois, S.; Jongmans, D.; Pirard, E.; Loke, M. Image processing of 2D resistivity data for imaging faults. *J. Appl. Geophys.* **2005**, *57*, 260–277. [CrossRef]

85. Singh, U.; Das, R.; Hodlur, G. Significance of Dar-Zarrouk parameters in the exploration of quality affected coastal aquifer systems. *Environ. Geol.* **2004**, *45*, 696–702. [CrossRef]

86. Hasan, M.; Shang, Y.; Akhter, G.; Jin, W. Delineation of contaminated aquifers using integrated geophysical methods in Northeast Punjab, Pakistan. *Environ. Monit. Assess.* **2020**, *192*, 12. [CrossRef]

87. Mahmud, S.; Hamza, S.; Irfan, M.; Huda, S.N.-U.; Burke, F.; Qadir, A. Investigation of groundwater resources using electrical resistivity sounding and Dar Zarrouk parameters for Uthal Balochistan, Pakistan. *Groundw. Sustain. Dev.* **2022**, *17*, 100738. [CrossRef]

88. Edwards, R.; Nobes, D.; Gomez-Trevino, E. Offshore electrical exploration of sedimentary basins; the effects of anisotropy in horizontally isotropic, layered media. *Geophysics* **1984**, *49*, 566–576. [CrossRef]

89. Mastrocicco, M.; Vignoli, G.; Colombani, N.; Zeid, N.A. Surface electrical resistivity tomography and hydrogeological characterization to constrain groundwater flow modeling in an agricultural field site near Ferrara (Italy). *Environ. Earth Sci.* **2010**, *61*, 311–322. [CrossRef]